

Structural and Electrochemical Characteristics of Ca-Doped “Flower-like” $\text{Li}_4\text{Ti}_5\text{O}_{12}$ Motifs as High-Rate Anode Materials for Lithium-Ion Batteries

Lei Wang,^{†,¶,||} Yiman Zhang,^{†,¶,||} Haoyue Guo,[†] Jing Li,^{‡,§} Eric A. Stach,^{‡,§,||} Xiao Tong,[§] Esther S. Takeuchi,^{†,‡,||} Kenneth J. Takeuchi,^{†,‡} Ping Liu,^{⊥,||} Amy C. Marschilok,^{*,†,‡,||} and Stanislaus S. Wong^{*,†,‡,||}

[†]Department of Chemistry, State University of New York at Stony Brook, Stony Brook, New York 11794-3400, United States

[‡]Department of Materials Science and Chemical Engineering, State University of New York at Stony Brook, Stony Brook, New York 11794-2275, United States

[§]Center for Functional Nanomaterials, Brookhaven National Laboratory, Building 480, Upton, New York 11973, United States

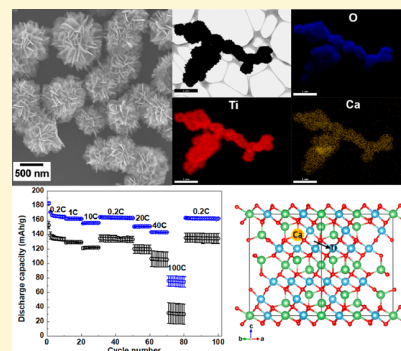
^{||}Energy Sciences Directorate, Brookhaven National Laboratory, Building 734, Upton, New York 11973, United States

[⊥]Chemistry Division, Brookhaven National Laboratory, Building 555, Upton, New York 11973, United States

[#]Condensed Matter Physics and Materials Sciences Division, Brookhaven National Laboratory, Building 480, Upton, New York 11973, United States

Supporting Information

ABSTRACT: Doped motifs offer an intriguing structural pathway toward improving conductivity for battery applications. Specifically, Ca-doped, three-dimensional “flower-like” $\text{Li}_{4-x}\text{Ca}_x\text{Ti}_5\text{O}_{12}$ (“ x ” = 0, 0.1, 0.15, and 0.2) micrometer-scale spheres have been successfully prepared for the first time using a simple and reproducible hydrothermal reaction followed by a short calcination process. The products were experimentally characterized by means of X-ray diffraction (XRD), transmission electron microscopy (TEM), scanning electron microscopy (SEM), energy dispersive spectroscopy (EDS) mapping, inductively coupled plasma optical emission spectrometry (ICP-OES), X-ray photoelectron spectroscopy (XPS), cyclic voltammetry (CV), electrochemical impedance spectroscopy (EIS), and galvanostatic charge–discharge testing. Calcium dopant ions were shown to be uniformly distributed within the LTO structure without altering the underlying “flower-like” morphology. The largest lattice expansion and the highest Ti^{3+} ratios were noted with XRD and XPS, respectively, whereas increased charge transfer conductivity and decreased Li^+ -ion diffusion coefficients were displayed in EIS for the $\text{Li}_{4-x}\text{Ca}_x\text{Ti}_5\text{O}_{12}$ (“ x ” = 0.2) sample. The “ x ” = 0.2 sample yielded a higher rate capability, an excellent reversibility, and a superior cycling stability, delivering 151 and 143 mAh/g under discharge rates of 20C and 40C at cycles 60 and 70, respectively. In addition, a high cycling stability was demonstrated with a capacity retention of 92% after 300 cycles at a very high discharge rate of 20C. In addition, first-principles calculations based on density functional theory (DFT) were conducted with the goal of further elucidating and understanding the nature of the doping mechanism in this study. The DFT calculations not only determined the structure of the Ca-doped $\text{Li}_4\text{Ti}_5\text{O}_{12}$, which was found to be in accordance with the experimentally measured XPD pattern, but also yielded valuable insights into the doping-induced effect on both the atomic and electronic structures of $\text{Li}_4\text{Ti}_5\text{O}_{12}$.



1. INTRODUCTION

The study of spinel type $\text{Li}_4\text{Ti}_5\text{O}_{12}$ (LTO) has received significant attention as a promising alternative to conventional graphite anode materials associated with lithium-ion batteries (LIBs) for applications including but not limited to the power sources of electric vehicles (EVs) and hybrid electric vehicles (HEVs).^{1,2} These materials possess a relatively high insertion potential of 1.55 V (vs Li/Li^+),³ which can minimize the chance of lithium dendrite formation and suppress the reduction of the electrolyte on the surface of electrode.⁴ In addition, LTO electrodes often maintain excellent structural stability, good

reversibility, and outstanding cyclability characteristics, which stem from their intrinsic ability to accommodate for the presence of lithium ions without significant structural change (i.e., zero-strain) during charge and discharge operations.^{3,4}

Although LTO possesses a lot of promise, its electrochemical performance and practical applications are still limited, due to its inherently poor electronic conductivity (10^{-13} – 10^{-9} S/

Received: September 11, 2017

Revised: December 15, 2017

Published: January 22, 2018

cm),⁵ relatively sluggish diffusion coefficients of lithium ions (estimated to be in the range of 10^{-8} – 10^{-13} cm²/s),⁶ and low energy density.⁷ Mitigating for these issues requires rationally exploiting changes in chemical composition and/or morphology to improve and fundamentally tune the rate performance of LTO. Such strategies include but are not limited to nanostructuring,^{8–14} surface coating,¹⁴ and ionic doping.¹ For instance, reducing the particle size within these nanostructures can potentially shorten the distance associated with electron conduction and Li⁺-ion transport. Furthermore, surface coating with either conductive carbon materials^{15–17} or metal nanoparticles¹⁷ can enhance the electronic conductivity between LTO particles, although it cannot necessarily alter the intrinsic conductivity of LTO.

The use of ionic doping in particular can effectively modify the intrinsic electronic conductivity and/or Li⁺-ion diffusion coefficients within LTO structures, thereby leading to higher capacities and improved rate capabilities. The advantages associated with the ion doping of LTO are several-fold. First, LTO is relatively insulating, due in part to the empty 3d orbital of Ti⁴⁺.¹⁸ Hence, doping ions with higher oxidation states might potentially drive the partial transformation of Ti⁴⁺ into Ti³⁺, based upon charge compensation considerations, because the concentration of electrons within the 3d orbitals can be therefore increased, a consequence of which is enhanced conductivity.¹⁹ Second, doping ions with a larger radius could potentially induce a lattice expansion, which may reduce the amount of lithium-ion diffusion blockage and thereby increase the ion conductivity of LTO.²⁰ Normally, the chosen dopant ions (i) should be either physically larger than the substituted ion, representing a strategy that can enhance the lithium-ion diffusion by means of lattice expansion, and/or (ii) should possess higher oxidation states than that of the substituted ions themselves, denoting an approach that can increase electron density by driving the ionic transformation from Ti⁴⁺ to Ti³⁺.

The cubic spinel LTO structure can be described in terms of the notation of [Li]_{8a}[LiTi₅]_{16d}[O]₁₂]_{32e} within the *Fd3m* space group. In this structure, 75% of Li⁺ ions occupy the tetrahedral 8a sites. The remaining Li⁺ ions and all of the Ti⁴⁺ ions reside at octahedral 16d sites, whereas O²⁻ ions constituting a cubic-close-packed array are located at 32e sites.²¹ The three-dimensional 8a–16c–8a network has been identified as the predominant Li⁺-ion transport pathway, due to a shorter diffusion distance and the presence of more available reactive sites.²² When intercalating lithium, the Li⁺ ions situated at the 8a sites together with the same amount of external Li⁺ ions likely shift to octahedral 16c sites to generate a “rock salt-type” structure, i.e., [Li]₆[LiTi₅]_{16d}[O]₁₂]_{32e}. When deintercalating lithium ions, this process is reversed. The three-dimensional [LiTi₅]_{16d}[O]₁₂]_{32e} spinel framework is extremely robust during the charge and discharge processes, thereby leading to a less than 0.1% difference in terms of lattice parameters.⁵

Though there has been prior research involving doping of either the [Li]_{8a}, [Li]_{16d}, [Ti]_{16d}, or [O]_{32e} sites, with ions such as Ni²⁺, Mg²⁺, Zn²⁺, Al³⁺, Pr³⁺, Cr³⁺, Zr⁴⁺, Nb⁵⁺, V⁵⁺, Ta⁵⁺, and F⁻,^{20,23} these previous studies have focused mainly on LTO characterized by either zero-dimensional nanoparticles,²⁴ one-dimensional nanofibers,^{4,25} or two-dimensional nanosheet^{26,27} morphologies. To the best of our knowledge, no prior investigations have focused on the ionic doping of a more complex three-dimensional hierarchical LTO motif. Furthermore, most of these earlier reports only provided data on the electrochemical performance of these doped LTO materials

with limited structural insights concerning the actual prospective doping site(s) from either an experimental or theoretical perspective.

It should be noted that a few groups have sought to probe the cation doping sites by either Rietveld refinement of Cu K α X-ray diffraction data or DFT calculations. For instance, refinements have been conducted on doped LTO species by fixing the positions of the Fe²⁺/Cr³⁺ dopant ions at the 16d sites as well as the Li⁺ and Ti⁴⁺ ions at both 8a and 16d sites, respectively.³ However, although this is a plausible approach, it is still nevertheless subject to constraints, due to the limited occupancy information available from the Cu K α X-ray diffraction data set. Specifically, it should be noted that this refinement method could not completely determine the nature of the cation doping, because of somewhat restrictive assumptions about the initial doping localization at the 16d site. A separate analysis of Gd³⁺-doped LTO materials used DFT calculations to compare two possible structures with dopants spatially confined to either the [Li]_{16d} site or the [Ti]_{16d} site; it was plausibly determined that doping of the [Ti]_{16d} site represented the more thermodynamically stable phase.²⁸

Investigations of Ca-doped LTO structures as anode materials are limited, and to the best of our knowledge, only three previous studies exist.^{29–31} Zhang et al.³⁰ reported on a series of micrometer-sized Ca-doped LTO particles (overall diameters of 1–2 μ m) with the chemical formula of Li_{4-x}Ca_xTi₅O₁₂ (“x” = 0, 0.05, 0.1, 0.15, and 0.2) through a solid-state reaction. The Ca dopants were deduced to occupy the [Li]_{8a} site, based on an increase in the cubic unit cell parameter “a” after Ca²⁺ doping, because the radius of Ca²⁺ is perceptibly larger than that of Li⁺ ions. Improved electrochemical performance for Ca-doped LTO materials was observed at higher charge–discharge rates, an observation that could be attributed to the improved electronic conductivity. The “x” = 0.1 electrode exhibited the highest electronic conductivity and fastest lithium-ion diffusivity, thereby demonstrating the best rate capability by delivering 122.4 mAh/g at 20C. The same group²⁹ also put together a combined theoretical and experimental study of Ca-doped LTO nanoscale spheres (measuring 100–200 nm in diameter), generated by a sol–gel method. It was found that these materials could deliver a specific capacity of 155.1 mAh/g at 10C, after 1000 cycles. DFT calculations in this work suggested that the Ca dopant preferably occupied the [Li]_{16d} site as opposed to the [Li]_{8a} site. Finally, Setiawan et al.³¹ synthesized a series of Ca-doped LTO samples using waste eggshells as the Ca source, through a solid-state reaction. Cyclic voltammetry characterization data indicated that Li_{4-x}Ca_xTi₅O₁₂ (“x” = 0.05) demonstrated the highest charge and discharge capacity of 177.14 and 181.92 mAh/g, respectively, measured with a scan rate of 100 μ V/s. However, it should be noted that insufficient relevant details on either a clear morphological motif or the nature of the Ca occupancy were provided within this most recent paper.

Hence, as compared with all of the previous work on the Ca-LTO system, the elements of novelty of our current study presented can be systematically summarized as follows. First, the morphology of the LTO samples generated within the three prior studies either possessed a “zero-dimensional” shape^{29,30} or was unknown to the degree that it was neither properly documented nor discussed.³¹ By contrast, within the present study, therefore, we report for the first time on the calcium

doping of a novel three-dimensional “flower-like” LTO motif. Second, none of these three previous reports investigated the electrode performance of Ca-doped LTO at high discharge and charge rates above 20C, denoting data critical for practical applicability. In our current study, we explicitly targeted the high-rate performance of the resulting Ca-LTO materials at 20C, 40C, and 100C, respectively. Third, within the current manuscript, we presented the successful *in situ* Ca-doping of the three-dimensional “flower-like” LTO anode material ($\text{Li}_{4-x}\text{Ca}_x\text{Ti}_5\text{O}_{12}$), prepared by a facile and controllable hydrothermal synthesis. The synthesis method we have reported herein is different and distinctive from either the solid-state or sol–gel method utilized in these previous reports. Last but not least, the precise nature of the Ca dopant occupancy within the first two of these prior reports remained controversial, whereas the last published paper cited did not provide any details whatsoever on the possible occupancy of Ca dopants. By contrast, within the current paper, we attempt to painstakingly shed light upon the exact Ca doping mechanism through a combined experimental and theoretical study.

Hence, at a fundamental level, to understand and correlate the effect of doping with respect to the resulting electrochemical performance within materials in general, it is crucial to further analyze and more thoroughly elucidate the Ca doping mechanism within the LTO motif itself, used as a model example. In the present study, therefore, we report for the first time on the calcium doping of a novel three-dimensional “flower-like” LTO motif with the explicit objectives of not only improving charge transfer within the LTO motif but also shedding light upon the exact doping mechanism. Herein we present the successful *in situ* Ca-doping of the three-dimensional “flower-like” LTO anode material ($\text{Li}_{4-x}\text{Ca}_x\text{Ti}_5\text{O}_{12}$), prepared by a facile and controllable hydrothermal synthesis. We investigated four different Ca doping molar ratios with “ x ” = 0, 0.1, 0.15, and 0.2. The effects of Ca^{2+} -ion doping upon the structure, morphology, and electrochemical characteristics of LTO were systematically investigated.

In this report, fitting of synchrotron X-ray diffraction data of “ x ” = 0.2 Ca^{2+} -doped material was conducted to determine the exact nature of the dopant site within the cubic LTO structure using the Rietveld method. Furthermore, DFT calculations were carried out to determine the exact nature of the preferred doping site within the hexagonal structure. Notably, the hexagonal structure was derived from the asymmetric unit of the cubic lattice. Lastly, the DFT-optimized structure was used as a more appropriate model for Rietveld refinement to confirm that the structure derived from theoretical DFT calculations was in fact consistent with the complementary experimental data.

Why is there an emphasis on this synergistic strategy of combining Ca-ion doping with a unique 3D hierarchical “flower-shape” structural design? First, calcium is a highly abundant and relatively inexpensive dopant; it possesses a Pauling’s crystal radius of 114 pm. This ion is larger than those of $[\text{Li}]_{16d}$ (i.e., 90 pm radius) and $[\text{Li}]_{8a}$ (i.e., 73 pm radius), respectively. Therefore, doping with Ca^{2+} could induce an optimal lattice expansion, thereby contributing to a better rate performance of this system.^{30,32} Second, the higher oxidation state of Ca^{2+} will result in the transformation of Ti^{4+} to Ti^{3+} due to charge compensation effects. This strategy should lead to the presence of more electrons in the Ti 3d orbital, and hence an enhanced electronic conductivity of the LTO itself. Third, the

novel hierarchical “flower-like” LTO microspheres, generated by our group recently,³³ consist of thin “sawtooth”-shaped constituent nanosheets, providing for not only shortened Li-ion diffusion distances but also enhanced contact area with electrolyte. In effect, the overall micrometer-scale spherical assemblies themselves should give rise to not only outstanding thermodynamic stability but also high tap density.^{13,34}

2. EXPERIMENTAL SECTION

2.1. Synthesis of Ca-Doped “Flower-like” LTO Micrometer-Scale Spheres. A typical synthesis of pure “flower-like” LTO microspheres has been previously reported by our group.³³ For the Ca-doped LTO materials, an appropriate amount of calcium acetate hydrate (Sigma-Aldrich, 99%) was added as the dopant source. In brief, ~40 pieces of Ti foil (Strem Chemicals, 99.7%), measured as 1 cm × 1 cm squares, were placed within a 120 mL autoclave with 86.1 mL of 0.5 M LiOH (Acros Organics, 98%) and 7.83 mL of 30% (w/w) H_2O_2 (VWR) aqueous solution, followed by strong stirring at room temperature for 15 min. Thereafter, relevant quantities of calcium acetate hydrate, calculated according to the doping molar ratio, were added to the autoclave, followed by additional stirring for 15 min. Subsequently, the as-prepared mixture solution was reacted at 130 °C for 4 h. The as-formed white precipitate was separated by vacuum filtration, washed with aliquots of deionized water as well as with ethanol, and ultimately oven-dried at 80 °C. The final products were annealed at 600 °C in air for 4 h in a muffle furnace in order to obtain the desired “flower-like” Ca-doped LTO microspheres.

2.2. Structural Characterization. X-ray Diffraction (XRD). Crystallographic data on both the undoped as well as the Ca-doped LTO micrometer-scale spheres were obtained using a Rigaku Miniflex II diffractometer, operating in the Bragg configuration using Cu $K\alpha$ radiation (1.54 Å). Specifically, diffraction data were collected in the range of 10° to 70° at a scanning rate of 1° per minute using a zero-background holder. A Rietveld refinement has been performed on as-obtained XRD profiles using the EXPGUI interface in the Match! (Crystal Impact GbR) software, thereby allowing for phase identification from the powder diffraction data. Synchrotron powder diffraction was performed at beamline 28-ID-1 (XPD-1) at the National Synchrotron Light Source-II (NSLS-II) at Brookhaven National Laboratory. The “ x ” = 0.2 Ca-doped sample was packed and sealed within a polyimide capillary tube for data acquisition. The X-ray wavelength was calibrated to 0.2388 Å with our LaB_6 standard. Diffraction measurements were collected using a 16-in. CsI scintillator. The two-dimensional data were integrated to simulate a one-dimensional pattern using GSAS-II software. The refinement was also conducted using the GSAS-II interface with the model generated from DFT calculations.

Elemental Composition Analysis. The actual Ca content within the doped LTO materials was determined using a Thermo Scientific iCAP 6000 Inductively Coupled Plasma Optical Emission Spectrometer (ICP-OES). The Ca-doped LTO samples were dissolved in nitric acid and analyzed at 317.9 nm, which is considered to be a sensitive and appropriate wavelength for the estimated determination of Ca content. The calibration curves for calcium, lithium, and titanium content, respectively, are shown in Figure S2. In addition, elemental mappings of Ti, O, and Ca within the LTO motif were collected using the energy dispersive spectrometer (EDS) associated with JEOL JEM-1400 instrument. Each elemental map was obtained after 60 scans.

Electron Microscopy. The structure, morphology, and size of the Ca-LTO micrometer-scale spheres were probed using an analytical high-resolution SEM (JEOL 7600F) instrument, operating at an accelerating voltage range of 15 kV and equipped with EDX capabilities. To prepare these samples for subsequent characterization, fixed quantities were dispersed in ethanol and sonicated for ~1 min, prior to their deposition onto an underlying silicon (Si) wafer. Low-magnification TEM characterization was performed on a JEOL JEM 1400 instrument at an accelerating voltage of 120 kV, with a 2048 × 2048 Gatan CCD Digital Camera. High-resolution TEM characterization results, including data associated with morphology and selected

area electron diffraction, were acquired with a JEOL JEM 2100F TEM instrument, equipped with a field-emission electron gun operating at 200 kV and a high-resolution pole-piece possessing a 0.19 nm point-to-point resolution. The camera length (L) was calibrated using an Au standard sample. The d -spacing values were extracted using the formula of $d = 2\lambda/LD$, wherein λ is the electron wavelength and D is the measured diffraction ring diameter. For sample preparation, a series of as-synthesized Ca-doped LTO samples were dispersed in ethanol and sonicated for 2 min to ensure a uniform dispersion. One drop of the solution was evaporated onto a 300 mesh Cu grid, which was coated with a lacey carbon film.

X-ray Photoelectron Spectroscopy (XPS). XPS analysis was performed to confirm the presence of Ca within the LTO material as well as to elucidate the oxidation states of the Ti within the doped samples. In particular, XPS samples were prepared by dispersing a series of Ca-doped LTO samples in ethanol. Aliquots of that solution were then dropped onto a Si wafer (measuring 1 cm \times 1 cm) followed by air drying. Samples were subsequently placed into the vacuum chamber of a home-built XPS surface analysis system, equipped with a model SPECS Phoibos 100 electron energy analyzer for electron detection. The chamber was evacuated to a low base pressure of about 2×10^{-10} Torr. XPS spectra were generated through the mediation of a Mg K α X-ray source ($h\nu = 1250$ eV) (model XR 50). The C 1s peak situated at 284.5 eV was set as a reference “standard”, in order to subsequently calibrate the respective locations of the Ti 2p peak and the Ca 2p peak. The linear background was then subtracted, and curve fitting was subsequently performed using the CasaXPS software.

2.3. Electrochemical Methods. Electrode Preparation. Electrodes were prepared using a slurry cast method with Ca-doped LTO as the active material, carbon, and polyvinylidene fluoride binder with an overall mass ratio of 85:10:5. Two electrode cells were assembled in an argon-filled glovebox using lithium metal as the counter electrode and 1 M LiPF₆ in 30/70 (v/v) ethylene carbonate and dimethyl carbonate solvent as the electrolyte.

Electrochemical Characterization. The electrochemical cells were tested in galvanostatic mode using voltage limits of 1.0 V for discharge and 2.5 V for charge. Cells were discharged using a series of rates ranging from 0.2 to 100 C, wherein 175 mAh/g was used as the capacity for all active materials in calculating the effective C rates. Cyclic voltammetry was utilized in the voltage window of 1.0–3.0 V at scan rates of 0.5, 1.0, 2.0, 4.0, and 5.0 mV/s, respectively.

Electrochemical impedance spectroscopy (EIS) measurements were carried out using a two-electrode configuration wherein lithium metal served as the reference and the counter electrode using a Biologic electrochemical workstation with a ± 10 mV ac signal and a frequency range from 10^5 to 20 Hz at a temperature of 30 °C. The effective diffusion coefficient D_{Li^+} for each type of material was determined from data in the range of 400 to 40 Hz.

2.4. Theoretical Modeling Methods. DFT Calculations. DFT implemented in the Vienna ab initio simulation package (VASP) was employed,³⁵ using the PAW potential³⁶ and GGA-PBE exchange-correlation functional.³⁷ In accordance with previous studies, the kinetic energy cutoff was set to 580 eV, and a Hubbard U correction term of $U_{\text{eff}} = 4$ eV was applied to the Ti d orbitals.³⁸ The Gaussian smearing method with Blöchl corrections was used with the total energies allowed to converge to a “resolution” better than 10^{-4} eV. The first Brillouin zone was sampled using a $3 \times 3 \times 3$ k-mesh. The pristine LTO crystal structure was modeled using a hexagonal supercell, which included eight formula units.³⁹ The DFT-optimized lattice parameters (8.46 Å) were found to be in good agreement with the value measured experimentally (namely 8.35 Å).⁴⁰ To determine the nature of the occupancy of the Ca dopants, a number of possible sites was considered. Only the most stable configuration was chosen from the DFT calculations for subsequent fitting to the measured XRD patterns.

3. RESULTS AND DISCUSSION

3.1. Structure and Composition Analysis. XRD spectra of our as-prepared doped $\text{Li}_{4-x}\text{Ca}_x\text{Ti}_5\text{O}_{12}$ (“ x ” = 0, 0.1, 0.15,

and 0.2) samples as well as a comparison of the (111) peak region for these materials are plotted in Figure 1. All of the

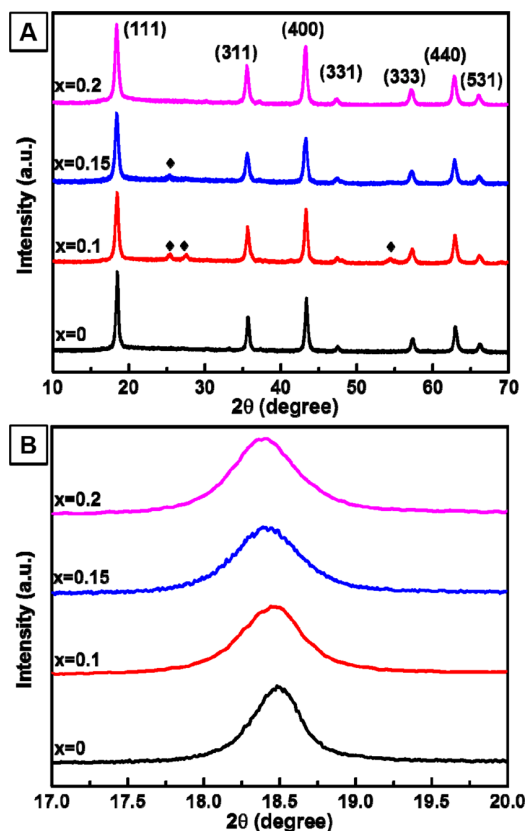


Figure 1. (A) XRD spectra along with (B) a magnified comparison of the (111) peaks associated with samples of $\text{Li}_{4-x}\text{Ca}_x\text{Ti}_5\text{O}_{12}$ (“ x ” = 0, 0.1, 0.15, and 0.2). TiO_2 impurities are labeled with \blacklozenge .

diffraction peaks in Figure 1A are consistent with and can be ascribed to the standard cubic spinel structure with the $Fd\bar{3}m$ space group (JCPDS #49-0207) of the LTO, except for very small amounts of anatase and rutile TiO_2 impurities that we observed with the “ x ” = 0.1 and “ x ” = 0.15 samples. Based on our previous mechanistic study of LTO formation, the presence of a minute amount of particulate TiO_2 impurities within the undoped $\text{Li}_4\text{Ti}_5\text{O}_{12}$ may be ascribed to the insufficient quantity of LiOH reagent used during the initial stage of the hydrothermal reaction process.³³ No observable TiO_2 impurities were noted within the “ x ” = 0.2 sample, likely owing to a more than adequate concentration of Ca^{2+} ions present, which would have fully reacted with any as-generated, “early stage” TiO_2 intermediate species in the presence of LiOH. The (111) peak shifted to lower angles with increasing Ca-ion doping, suggesting that the doped LTO samples possess slightly larger lattice parameters than that of the undoped LTO. The exact amounts of impurities relative to the undoped LTO phase were analyzed using Rietveld refinement, and the relevant data are presented in Figure S1. No impurity peaks associated with CaTiO_3 were detected at “ x ” = 0.2, indicating that the doped Ca^{2+} ions were successfully incorporated within the lattice structure of LTO.

To analyze the nature of the Ca-ion doping effect as a function of dopant concentrations, the (111) peak in particular of LTO has been enlarged and highlighted in Figure 1B. The

(111) peak shifted to lower angles with increased Ca-ion doping, suggesting that the doped LTO samples possess slightly larger lattice parameters than that of the undoped LTO. In effect, according to the refinement results, the lattice parameters were calculated to be 8.354, 8.360, 8.364, and 8.366 Å, for the pure, Ca 0.1-, Ca 0.15-, and Ca 0.2-doped LTO samples, respectively. These findings can be ascribed to the fact that the larger Ca^{2+} (114 pm) ions plausibly replaced either the Li^+ (90 pm) at the 16d site or the Li^+ (73 pm) at the 8a site, coupled with the transformation of a certain amount of Ti^{4+} (61 nm) to Ti^{3+} (67 nm), due to charge compensation effects.³⁰ The expansion of lattice planes is likely beneficial for reducing barriers to Li-ion diffusion, denoting a viable means of increasing the ionic conductivity of LTO.

Rietveld refinement of the synchrotron X-ray diffraction data for the “ x ” = 0.2 sample was carried out to determine the nature of the Ca^{2+} cation doping site in the LTO $Fd\bar{3}m$ lattice. The visual fit for the “ x ” = 0.2 sample is displayed in Figure 2a,

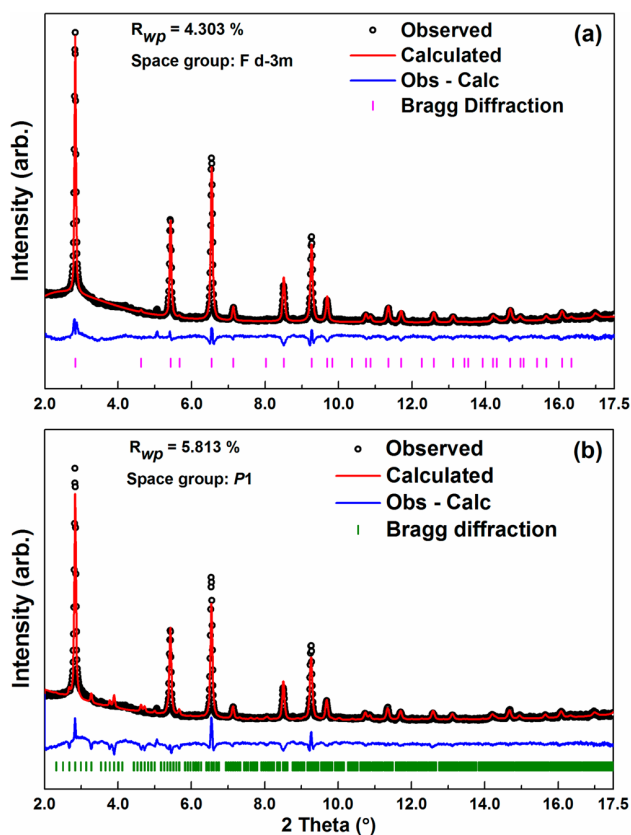


Figure 2. Rietveld refinement-based visual fit to synchrotron X-ray diffraction data of the “ x ” = 0.2 Ca-doped material using (a) the cubic structure with parameter $a = 8.3642$ Å coupled with (b) the DFT calculated structure corresponding to the $P1$ space group with unit cell parameters of $a = 11.8101$ Å, $b = 11.8101$ Å, $c = 11.8101$ Å, $\alpha = 89.95^\circ$, $\beta = 89.97^\circ$, and $\gamma = 119.99^\circ$.

wherein all Ca^{2+} cations were doped into the $[\text{Li}]_{16d}$ site with an occupancy of 0.033, which corresponded to a doping quantity of “ x ” = 0.2 Ca per LTO unit formula. After refinement, the lattice parameter “ a ” expanded from 8.360 to 8.364 Å. The atomic positions and occupancies after refinement using the $Fd\bar{3}m$ lattice are summarized in Table S1.

The morphologies and physical structures of the pure and doped LTO samples were studied by TEM, SEM, and HRTEM, respectively, as shown in Figures 3 and 4. All of

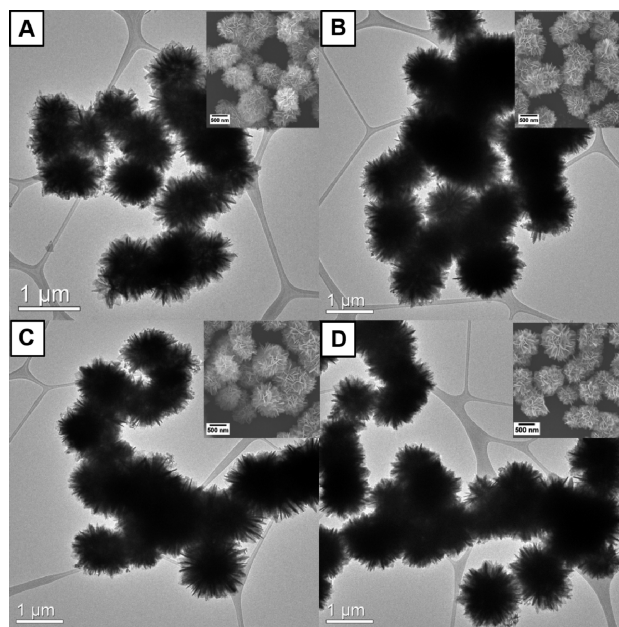


Figure 3. TEM and SEM (inset figures) images of (A) undoped LTO as well as with doped $\text{Li}_{4-x}\text{Ca}_x\text{Ti}_5\text{O}_{12}$ samples: (B) “ x ” = 0.1, (C) “ x ” = 0.15, and (D) “ x ” = 0.2.

the doped samples (Figure 3B–D and Figure 4d,g,j) retained a similar hierarchical “flower-shape” morphology as compared with that of the undoped LTO (Figure 3A and Figure 4a). Specifically, the distinctive “petal” regions of each of the three doped samples (Figure 4e,h,k) also retained a similar shape and geometric configuration to that of the undoped LTO (Figure 4b). Moreover, the crystallographic phases of all of the synthesized samples remained the same after doping, as shown in Figure 4c,f,i,l. All of the samples exhibited an overall monodisperse size distribution of $1 \mu\text{m}$, consisting of constituent petal-like component nanoscale sheets, each individually measuring 12.5 ± 2.6 nm in thickness.

With respect to the elemental composition analysis, samples were characterized with the use of ICP-OES, and these data provided information about the actual doping ratios within each of the Ca-doped LTO samples. The measured results suggest that the Li-to-Ca ratio within each $\text{Li}_{4-x}\text{Ca}_x\text{Ti}_5\text{O}_{12}$ sample was experimentally found to be 3.69:0.09, 3.62:0.14, and 3.67:0.22, when working with “apparent” doping ratios of “ x ” = 0.1, 0.15, and 0.2, respectively, wherein the Ti content was stoichiometrically assigned as 5. To ascertain the elemental spatial distribution of dopants within the LTO motif, EDS mapping images based upon bright-field scanning transmission electron microscopy (STEM) of several LTO micrometer-scale spheres are provided in Figure 5. These data clearly confirm the elementally homogeneous distribution of calcium within the LTO lattice for samples prepared at each of the various doping levels.

X-ray photoelectron spectroscopy (XPS) was also utilized to investigate the chemical nature of the LTO micrometer-scale spheres, before and after calcium doping. XPS data associated with the Ti 2p spectra of the undoped as well as of the Ca-

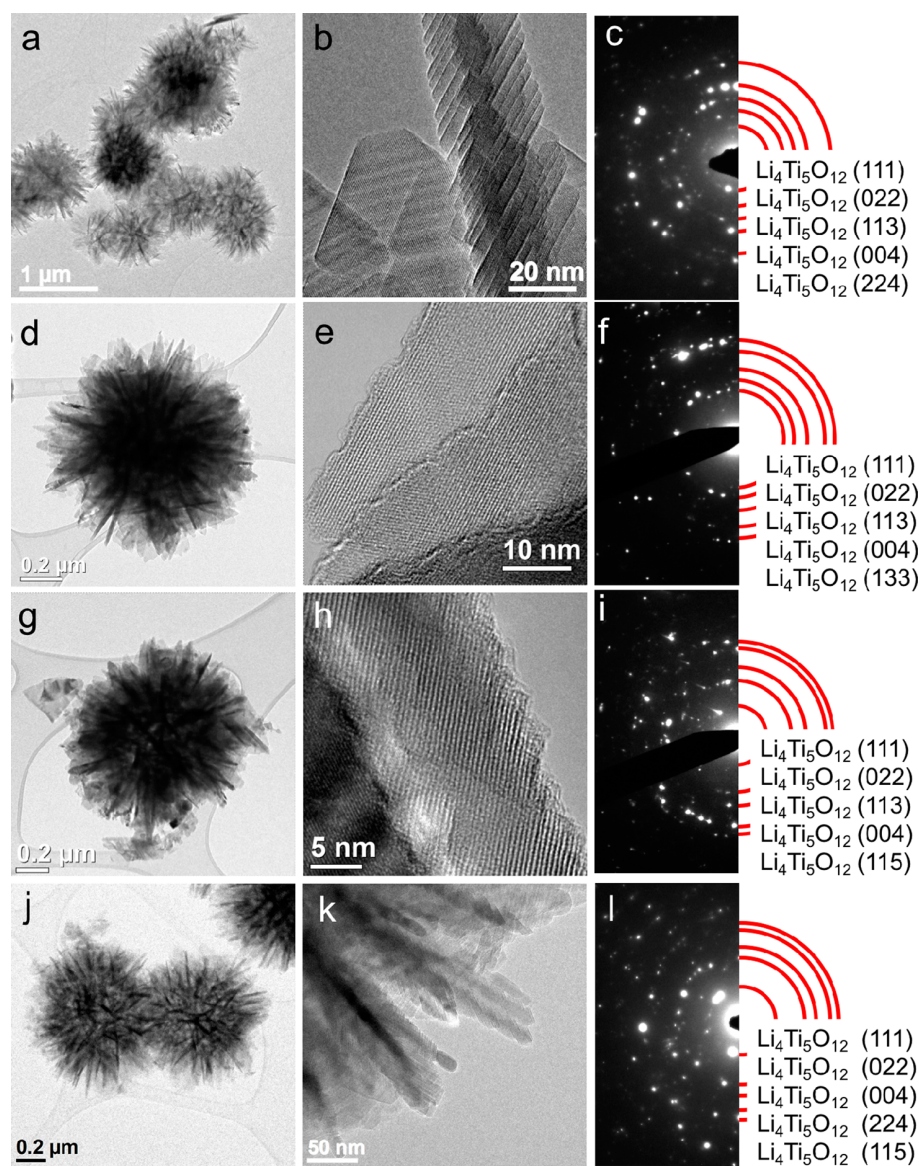


Figure 4. Morphology and phase characterization of (a–c) undoped LTO and doped LTO samples from (d–f) “ x ” = 0.1, (g–i) “ x ” = 0.15, and (j–l) “ x ” = 0.2, respectively.

doped LTO samples are presented in Figure 6. The fitted peak positions as well as the calculated ratios of $\text{Ti}^{4+}:\text{Ti}^{3+}$ for the various systems are displayed in Table 1. The undoped LTO micrometer-scale spheres (Figure 6A) yielded two sets of peaks, situated not only at (i) 457.6 and 463.2 eV, corresponding to the $2p_{3/2}$ and $2p_{1/2}$ peaks of Ti^{4+} , but also at (ii) 456.5 and 462.1 eV, associated with the $2p_{3/2}$ and $2p_{1/2}$ peaks of Ti^{3+} . These results imply that our as-synthesized, undoped LTO motifs incorporate self-doped Ti^{3+} species. Quantitatively, the ratio of $\text{Ti}^{4+}:\text{Ti}^{3+}$ was 1:0.245, a value derived from the corresponding areas of the fitted Ti^{4+} $2p_{3/2}$ and Ti^{3+} $2p_{3/2}$ peak regions.

A previous study on Ti^{3+} self-doped LTO nanosheets has reported that the introduction of Ti^{3+} species and/or oxygen vacancies may greatly improve the observed electronic conductivity. In fact, it was found that the Ti^{3+} self-doped LTO exhibited markedly improved lithium-ion storage performance, including higher specific capacities, superior rate

performance, and better cycling stability by comparison with LTO nanostructures containing no apparent Ti^{3+} dopants.²⁶

At the lower Ca-ion doping levels of “ x ” = 0.1 (Figure 6B) and “ x ” = 0.15 (Figure 6C), the analogous ratios of $\text{Ti}^{4+}:\text{Ti}^{3+}$ decreased to 1:0.149 and 1:0.130 (Table 1), respectively, denoting data that are noticeably lower than those of the undoped LTO sample. These results can be potentially ascribed to the presence of TiO_2 impurities within both samples, as corroborated by both the XRD spectra in Figure 1A and the corresponding refinement results in Figure S1; the implication is that there are more Ti^{4+} species within these samples as compared with the undoped LTO control.

By contrast, the trend with the “ x ” = 0.2 sample (Figure 6D) was reversed in that this sample appeared to have contained more Ti^{3+} ions as compared with its undoped LTO counterpart. In this case, the apparent ratio of $\text{Ti}^{4+}:\text{Ti}^{3+}$ was calculated to be 1:0.464 (Table 1). That is, the quantity of Ti^{3+} appeared to have notably increased within the “ x ” = 0.2 sample,

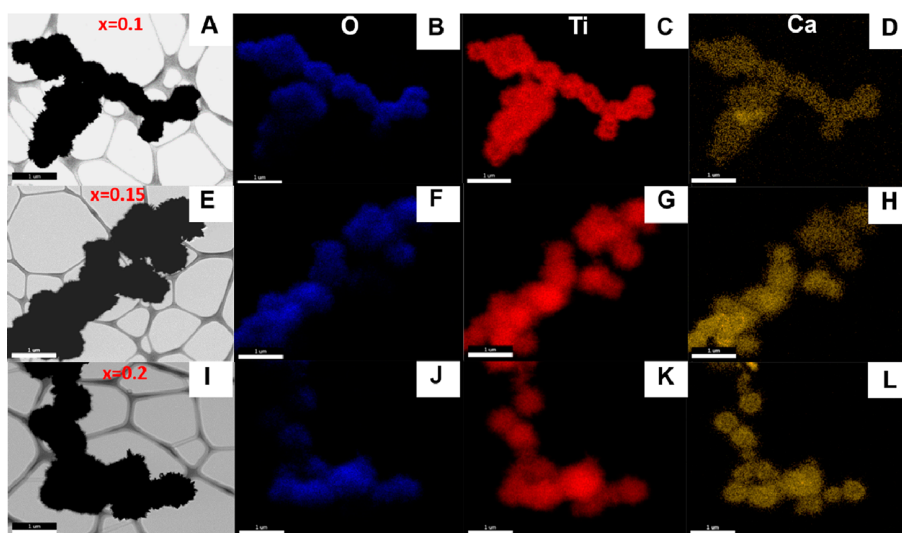


Figure 5. Bright-field STEM image (A, E, I), as well as elemental EDS mapping of the same region of LTO microspheres, highlighting the spatial chemical distribution of Ti (B, F, J), Ti (C, G, K), and Ca (D, H, L) recorded on $\text{Li}_{4-x}\text{Ca}_x\text{Ti}_5\text{O}_{12}$ samples: “ x ” = 0.1, 0.15, and 0.2, respectively. The scale bar is 1 μm in every image.

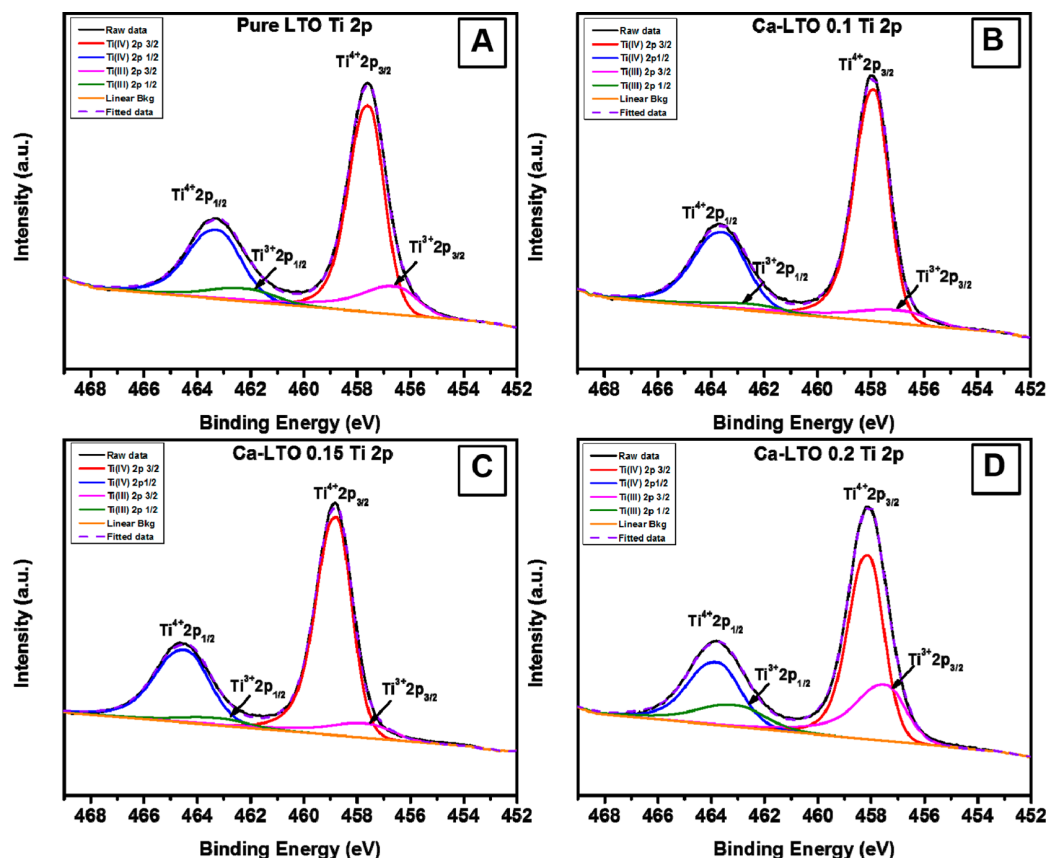


Figure 6. XPS Ti 2p spectra of (A) undoped LTO, and $\text{Li}_{4-x}\text{Ca}_x\text{Ti}_5\text{O}_{12}$ samples: (B) “ x ” = 0.1, (C) “ x ” = 0.15, and (D) “ x ” = 0.2, respectively.

thereby implying the most effective transformation from Ti^{4+} to Ti^{3+} observed of the materials tested. This finding was also directly connected to and associated with not only the largest amount of expected Ca incorporation for our sample but also the presence of the most “phase-pure” structure with no evident TiO_2 residual impurities. Therefore, we would expect to have measured the most enhanced electronic conductivity within the

“ x ” = 0.2 sample, because of the increase in the number of electrons associated with the formation of Ti^{3+} states, all of which would have led to the improved electrochemical properties observed.²⁶

3.2. DFT Calculations on $\text{Li}_{4-x}\text{Ca}_x\text{Ti}_5\text{O}_{12}$. DFT+U calculations were performed to determine the structure of Ca-doped LTO and to elucidate the doping-induced effect

Table 1. Peak Positions of $Ti^{4+} 2p_{3/2}$, $Ti^{4+} 2p_{1/2}$, $Ti^{3+} 2p_{3/2}$, and $Ti^{3+} 2p_{1/2}$, as well as the Ratios of $Ti^{4+}:Ti^{3+}$ within the Undoped LTO and Various Ca-Doped LTO Samples

Doping ratio	$Ti^{4+} 2p_{3/2}$ (eV)	$Ti^{4+} 2p_{1/2}$ (eV)	$Ti^{3+} 2p_{3/2}$ (eV)	$Ti^{3+} 2p_{1/2}$ (eV)	$Ti^{4+}:Ti^{3+}$
"x" = 0	457.6	463.2	456.5	462.1	1:0.245
"x" = 0.1	457.9	463.5	457.0	462.6	1:0.149
"x" = 0.15	458.8	464.4	457.6	463.2	1:0.130
"x" = 0.2	458.1	463.8	457.4	463.0	1:0.464

upon the corresponding intrinsic electronic structures of LTO. Previously, several structures have been employed to describe the structures of LTO and cation-doped LTO, including cubic,⁴¹ triclinic,^{28,29,42} and hexagonal³⁹ conformations, respectively. For cubic LTO, Cr^{3+} and Ni^{3+} mainly occupy the 16d sites, whereas Fe^{3+} and Mg^{2+} ions are predominantly localized at the 8a sites, which hinder Li^+ ion diffusion, according to the DFT calculations.⁴¹ Within a triclinic structure of LTO, Zn^{2+} ions prefer the $[Li]_{8a}$ sites.⁴² However, Gd^{3+28} and Ca^{2+29} ions favor the $[Li]_{16d}$ sites. It is plausible that the structures of LTO and of the corresponding species incorporating doped ions may both be essential for more definitively determining the structures of doped LTO.

In the present study, DFT calculations were performed first to determine the structure of the pristine LTO prior to experimental Ca-ion doping. Various models have been optimized using DFT with subsequent fitting to the measured XRD pattern. The results indicated that the hexagonal LTO (Figure 7a) matched best with our experimental XRD (R_{wp} =

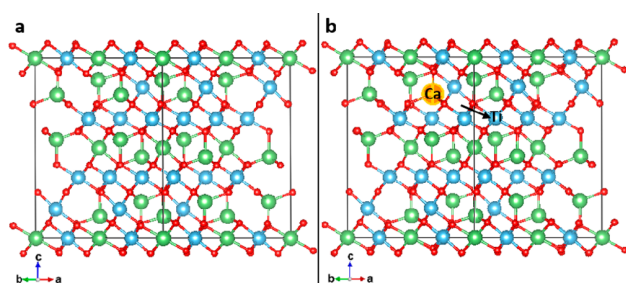


Figure 7. DFT-optimized structures of (a) a pristine hexagonal $(Li_4Ti_5O_{12})_8$ supercell and (b) a $(Ca_{0.125}Li_4Ti_5O_{12})_8$ supercell with Ca localized at the tetrahedral 8a site, wherein the positions of Ca^{2+} and the reduced Ti^{3+} on doping have been labeled (orange: Ca; green: Li; blue: Ti; black arrow referring to reduced Ti; red: O).

6.2%) as compared with either the corresponding cubic (R_{wp} = 6.863%) or triclinic (R_{wp} = 16%) structures. In the hexagonal cell structure, every sixth layer along the c axis is composed of solely Li ions. Li^+ ions occupy all of the tetrahedral 8a sites and 1/6 of the octahedral 16d sites, whereas Ti^{4+} ions take up the rest of the 16d sites. In addition, the octahedral 16c vacancies provide possible sites for Li insertion and diffusion.

Therefore, based upon an underlying hexagonal LTO structure, all of the possible sites for Ca-ion doping at "x" = 0.125 have been tested using DFT calculations. Our results highlight that by at least an energy level of 0.49 eV/ Ca^{2+} ion, Ca^{2+} ions prefer to substitute for the tetrahedral Li^+ ions at the 8a site (Figure 7b) rather than either replacing the Li^+/Ti^{4+} ions at the octahedral 16d or occupying the 16c vacancy sites. This substitution is energetically favorable with an energy gain

of 2.23 eV, considering an overall process of $Li_4Ti_5O_{12} + 0.125 Ca \rightarrow Ca_{0.125}Li_{3.875}Ti_5O_{12} + 0.125 Li$.

We also tested the effect of defects. According to the XPS measurements, oxygen vacancies were generated in the 32e sites of pristine LTO so as to form $Li_4Ti_5O_{11.5}$ (Figure S9), which cost an energy of 9.91 eV. However, the doped Ca^{2+} ions remained at the 8a site, which ended up being 0.32 eV/ Ca^{2+} ion more stable than a corresponding localization at the 16d sites. It is worth pointing out that our results are different from those of a previous study focused on triclinic LTO, wherein it was found that the octahedral 16d site was in fact preferred by Ca^{2+} ions.²⁹ That is, the positions of dopant metal ions can indeed vary, depending upon the structure of pristine LTO. The DFT-optimized $Ca_{0.125}Li_{3.875}Ti_5O_{14}$ structure fits well with the synchrotron XPD data for $Ca_{0.2}Li_4Ti_5O_{12}$ using Rietveld method, thereby resulting in a R_{wp} of 5.813% (Figure 2b). It is worth noting that the Rietveld refinement results based on cubic (Figure 2a) and hexagonal (Figure 2b) LTO structures are both reasonable, considering their relative small R_{wp} . Our refinement and DFT calculation results collectively suggested that the positions of dopant metal ions can indeed vary, depending upon the structure of pristine LTO. Specifically, within our current study, because the hexagonal LTO structure has been theoretically proven to be the best match for the experimental XPD results after DFT optimization, we conclude that the Ca^{2+} ions most likely occupy the 8a site.

We also probed the case wherein the Ca concentration is increased. For $Ca_{0.25}Li_{3.75}Ti_5O_{14}$, the Li 8a location remains the preferential site for the doped Ca^{2+} ions, and the fitting error to the XPD data for $Ca_{0.2}Li_4Ti_5O_{12}$ is only slightly increased to 6.172%. Furthermore, the cell volume expansion with respect to pristine LTO, given as $\frac{V-V_0}{V_0} \times 100\%$, is 0.74% after doping with Ca. This small expansion agrees well with the corresponding experimental XRD data (0.43%). With Ca^{2+} stabilized at the 8a sites, the diffusion network, 8a–16c–8a, for Li^+ ions is likely to be hindered, which thereby offers a plausible explanation for the experimentally observed decrease in the Li^+ diffusion rate (see section on EIS analysis).

In addition to evident atomic structure effects, significant changes in the electronic signature of LTO due to Ca-ion doping were also observed. According to our calculated projected electronic density of states (PDOS), the band gap of LTO is 2.10 eV, which is within the range of previous experimental and calculated values.²⁸ These results confirm that LTO is a typical insulator with low electronic conductivity. In pristine LTO, the valence bands were mainly composed of O 2p states, whereas the conduction bands were dominated by Ti 3d states (Figure 8a). The overlapping between Ti 3d and O 2p in terms of their electronic density of states suggested a strong O–Ti interaction mediated by the TiO_6 octahedral unit.

After Ca-ion doping (Figure 8b), however, a new Ti 3d state at the Fermi level emerged, and the band gap significantly decreased to 0.96 eV. Therefore, the electronic conductivity was enhanced. The Fermi level shifted toward the conduction bands, indicative of electron transfer from doped Ca to LTO. Ti^{4+} ions were identified as the electron acceptors. The Ti^{4+} ion, which was localized at the second nearest neighbor of the doped Ca^{2+} ions (Figure 8b), gave rise to a new state at the Fermi level in Ti 3d states after doping, which suggested a reduction to Ti^{3+} , whereas the other ions remained as Ti^{4+} (Figure 8c). Hence, Ti^{4+} and Ti^{3+} ions coexist in the Ca-doped LTO, in accordance with the XPS measurements. The presence

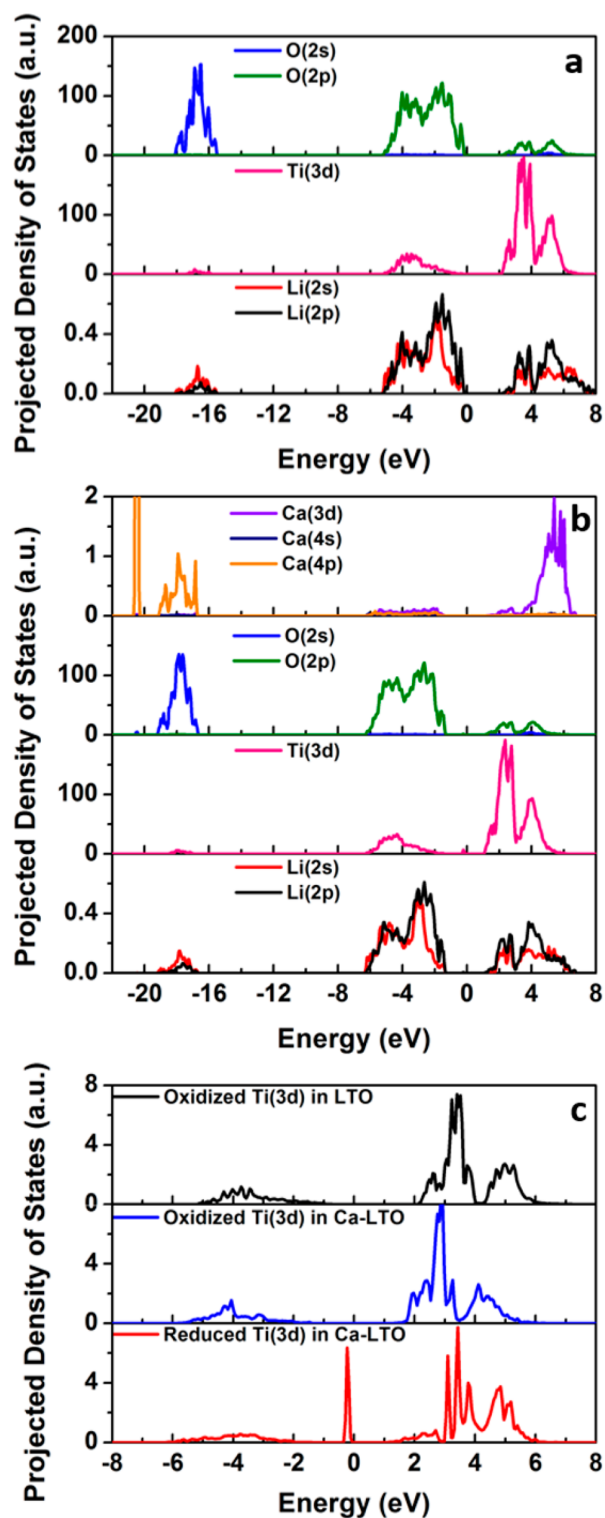


Figure 8. Projected electronic density of states (PDOS) of (a) pristine $\text{Li}_4\text{Ti}_5\text{O}_{12}$, (b) $\text{Ca}_{0.125}\text{Li}_4\text{Ti}_5\text{O}_{12}$ with Ca in tetrahedral 8a site, and (c) oxidized and reduced Ti ions within pristine $\text{Li}_4\text{Ti}_5\text{O}_{12}$ and $\text{Ca}_{0.125}\text{Li}_4\text{Ti}_5\text{O}_{12}$.

of reduced Ti^{3+} ions is likely to increase the observed electronic conductivity.

3.3. Electrochemical Properties of $\text{Li}_{4-x}\text{Ca}_x\text{Ti}_5\text{O}_{12}$ (“ x ” = 0, and 0.2) Samples. We found that the two Ca-doped

$\text{Li}_{4-x}\text{Ca}_x\text{Ti}_5\text{O}_{12}$ samples with “ x ” = 0.1 and 0.15 contained noticeable TiO_2 impurities. Hence, to rule out the effect of the TiO_2 impurities and to definitively explore the correlation between Ca-ion doping and the resulting electrochemical performance, we focus our discussion herein on a direct comparison between the behavior of phase-pure “ x ” = 0.2 Ca-doped LTO sample and the corresponding undoped pristine LTO control. The associated data for the “ x ” = 0.1 and 0.15 materials have been brought together in the [Supporting Information](#).

Rate Capability. Electrochemical evaluation of the response to a series of currents for the “ x ” = 0.2 Ca-doped LTO and the undoped samples are displayed in [Figure 9a](#). Data associated

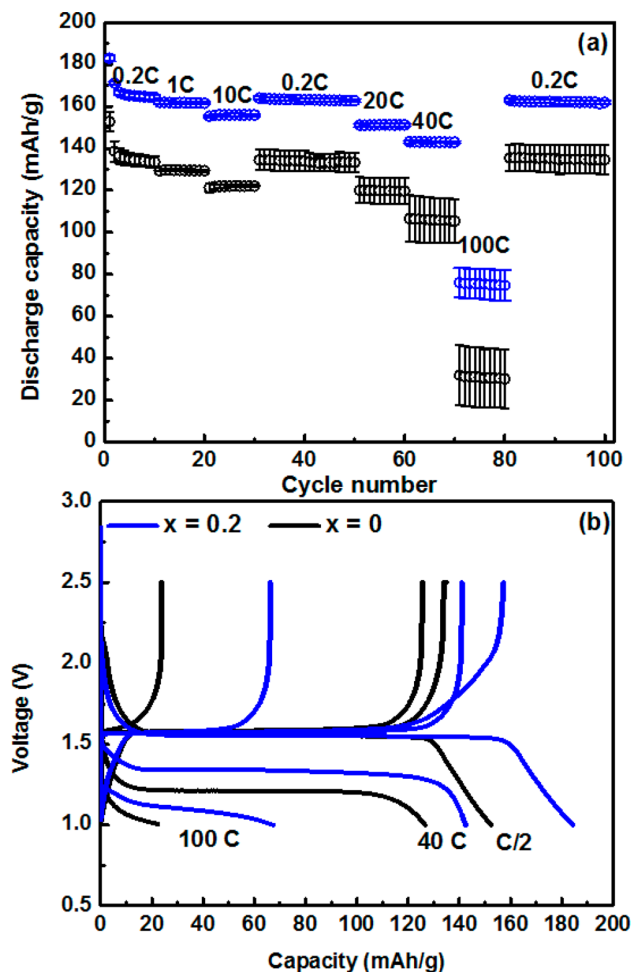


Figure 9. (a) Capacity values measured under a series of discharge rates for undoped and “ x ” = 0.2 Ca-doped $\text{Li}_{4-x}\text{Ca}_x\text{Ti}_5\text{O}_{12}$ based electrodes. (b) Discharge and charge curves at C/2 (cycle 1), 40C (cycle 70), and 100C rates (cycle 80) for “ x ” = 0.2 and undoped (“ x ” = 0) 3D “flower-like” LTO electrodes, respectively.

with the other two doped samples with “ x ” = 0.1 and 0.15 are presented in [Figure S3](#). All cells were subjected to 100 cycles, wherein the discharge/charge rates ranged from 0.2C to 100C. The data shown here denote average discharge capacities with standard deviations shown. By means of comparison, undoped LTO was also tested as a control sample using the same program.

The “ x ” = 0.2 Ca-doped LTO sample gave rise to the best rate capability and delivered capacities of 163, 151, 143, and 75 mAh/g under discharge rates of 0.2C, 20C, 40C, and 100C, at cycles 50, 60, 70, and 80, respectively. The electrodes created from samples with two other doping levels, i.e., “ x ” = 0.1 and 0.15, displayed similar discharge capacities of around 150, 138, 127, and 25 mAh/g at cycles 50, 60, 70, and 80, respectively. The undoped LTO material yielded the lowest capacities out of all of the samples measured, delivering only 133, 120, 105, and 30 mAh/g at cycles 50, 60, 70, and 80, respectively. In fact, the “ x ” = 0.2 electrode cells provided for not only ~15 mAh/g higher capacity than the other two Ca-doped materials possessing different doping levels, but also ~30 mAh/g higher capacity than the undoped LTO material, at rates of 0.2C, 1C, 10C, and 40C, respectively. Notably, the “ x ” = 0.2 sample yielded a three times higher capacity than the other three types of electrodes measured at 100 C. The capacity retention behavior was first assessed by considering the capacity obtained under a 0.2C discharge rate as a function of cycle number. Data implied that all materials gave rise to a 99% capacity retention from cycle 10 to cycle 100.

The discharge and charge curves at C/2 (cycle 1), 40C (cycle 70), and 100C (cycle 80) are highlighted in Figure 9b. As the discharge rate increased from C/2 to 40C, the voltage plateau for all materials correspondingly decreased from 1.56 to 1.32 V. Notably, at 100C, use of the “ x ” = 0.2 electrode led to a discharge curve with a capacity of 68 mAh/g and a voltage plateau at 1.1 V. It was noted that the Coulombic efficiencies measured during the first cycle were 86.5%, 90.1%, 85.3%, and 85.1% for the $\text{Li}_{4-x}\text{Ca}_x\text{Ti}_5\text{O}_{12}$ (“ x ” = 0, 0.1, 0.15, and 0.2) samples, respectively, which were lower than those of previously reported micrometer-sized LTO materials, which had demonstrated efficiencies ranging from 93% to 95%.^{43,44} Such observations likely originate from the unique “flower-like” morphology of our LTO motifs.^{45–47}

Several plausible explanations are provided herein in order to address this phenomenon associated with our material. First, in the first cycle, it is possible that a nontrivial amount of capacity was generated upon discharge beyond the 1.55 V redox plateau to 1.0 V. The relatively large capacity observed outside of the plateau is not reversible, as highlighted in Figure 9b, and it dramatically decreases after the first cycle, leading to the rather low initial Coulombic efficiency observed. Using XPS, Verde et al.⁴⁰ demonstrated that the presence of this irreversible capacity could be attributed to the reaction between nanoscale LTO motifs possessing high surface area-to-volume ratios and the electrolyte itself, leading to overlithiation (and subsequent structural distortion) of LTO itself from 1.5 to 1.0 V. To back up this assertion, significant changes in the surface morphology and conductivity of LTO upon discharge beyond the 1.55 V redox plateau to 1.0 V were observed using conductive atomic force microscopy. It is worth highlighting that the Coulombic efficiency immediately improved in subsequent cycles, gradually increasing to nearly 99% for all four of our “flower-like” LTO samples by the 10th cycle and beyond.

Our as-synthesized 3D “flower-like” LTO electrode has been previously reported to exhibit a favorably high rate performance.³³ By doping with calcium, the rate capability was apparently enhanced as compared with the undoped LTO material. Specifically, the “ x ” = 0.2 doping ratio sample had been confirmed to outperform analogues with “ x ” = 0.1 and “ x ” = 0.15 ratios. Especially when compared with other doped LTO systems, our “flower-like”, Ca-doped (“ x ” = 0.2) material

provided for higher capacities, particularly at high discharge rates of 20C and 40C, delivering 151 and 143 mAh/g, respectively.

As mentioned earlier, Zhang et al.³⁰ reported on a series of Ca-doped particles with doping ratios ranging from “ x ” = 0.05 to “ x ” = 0.2, and it turned out the “ x ” = 0.1 electrode possessed the best rate capability with a value of 123.4 mAh/g at 20C. Moreover, their spherical Ca-doped LTO motifs delivered a 158 mAh/g capacity at 10C. Elements such as Zr^{4+} ,⁴⁸ Gd^{3+} ,²⁸ Sc^{3+} ,⁴⁹ and Sm^{3+} ⁵⁰ have also been extensively studied as potential cationic dopants for LTO. For example, 0.05 Zr^{4+} -doped LTO highlighted a capacity of 120 mAh/g at 30C, whereas the 0.1 and 0.15 doping levels maintained a capacity of 108 mAh/g at 30C. We should note that none of these materials were tested at as a high rate above 40C, which was specifically studied here in our current manuscript. A detailed comparison of our results with prior literature is summarized in Table 2.

Cycling Performance. All samples were subjected to a galvanostatic cycling test for 300 cycles at 20C discharge and 1C charge rates using 1.0 and 2.5 V for the discharging and the charging voltage limit, respectively. Figure 10 displays the discharge capacity versus cycle number at 20C for the 300 cycles of testing for undoped and “ x ” = 0.2 Ca-doped LTO materials, respectively. For an electrode possessing a Ca-ion dopant level of “ x ” = 0.2, the delivered capacity was higher than that of the other two doping levels (Figure S4) as well as of the undoped LTO electrodes through all cycles. In effect, we measured capacities of 164 mAh/g at cycle 1, 154 mAh/g at cycle 100, and 151 mAh/g at cycle 300 with a capacity retention of 94% and 92% for cycle 100 and 300, respectively. By contrast, “ x ” = 0.1 and “ x ” = 0.15 Ca-doped electrodes demonstrated 90% retention by delivering capacity values of 153 mAh/g (cycle 1), 137 mAh/g (cycle 300) as well as 155 mAh/g (cycle 1), and 141 mAh/g (cycle 300), respectively.

When comparing these results with those of previously reported Ca-doped materials, the best performance was associated with a 93% capacity retention after 100 cycles at 1 C. It is clear that all our Ca-doped LTO materials exhibited excellent capacity retention, even at as high a rate as 20 C. The discharge and charge curves for “ x ” = 0, “ x ” = 0.1, “ x ” = 0.15, and “ x ” = 0.2 electrodes at cycles 1, 2, 8, and 10 are provided in Figure S6. The charge capacity as a function of cycle number is shown in Figure S7, and manifests a similar trend with the discharge capacity performance. The initial charge capacity was 133, 146, 149, and 157 mAh/g, whereas the capacity delivered after 300 cycles was 100, 137, 141, and 151 mAh/g, corresponding to a charge capacity retention of 75%, 93.8%, 94.6%, and 96.2%, for the undoped, “ x ” = 0.1, 0.15, and 0.2 samples, respectively. The “ x ” = 0.2 sample clearly delivered the highest charge capacities as well as the most stable cycling performance at a 1C charge rate among all of the samples analyzed.

Cyclic Voltammetry. Results are provided in Figure 11 (“ x ” = 0.2) and Figure S5 (“ x ” = 0.1 and 0.15). The linear fits of the peak current (i_p) as a function of the square root of the scan rate for each type of cell are shown in Figure S8. All of these results demonstrated correlation coefficients close to 0.999, which imply a diffusion controlled behavior for all of the cells. Cathodic peak positions at cycle 1 for “ x ” = 0.1, 0.15, and 0.2 electrodes were noted at (1.417 V, −1925.71 mA/g), (1.405 V, −1998.51 mA/g), and (1.444 V, −2652 mA/g), whereas the corresponding anodic peak positions at cycle 1 were found at

Table 2. Rate Capability and Cycling Stability of the Ca-Doped $\text{Li}_{4-x}\text{Ca}_x\text{Ti}_5\text{O}_{12}$ Electrode Prepared in This Work as well as of Those of Analogous Doped LTO Materials Reported in Previous Studies

Dopant	Material	Morphology	Method	Rate capability	Cycling performance	ref
Ca	$\text{Li}_{4-x}\text{Ca}_x\text{Ti}_5\text{O}_{12}$ (" x " = 0, 0.1, 0.15, 0.2) (cycle between 2.5 and 1.0 V)	Flowers: overall diameter: 1 μm ; petal thickness: 12 nm	Hydrothermal at 130 °C for 4 h + annealing at 500 °C for 3 h	" x " = 0.2, 163, 151, 143, 75 mAh/g under 1C, 20C, 40C, and 100C	" x " = 0.2, at 0.2C, 99% retention from cycle 10 to cycle 100; at 20C, 92% retention after 300 cycles	our work
	$\text{Li}_{3-x}\text{Ca}_x\text{Ti}_5\text{O}_{12}$ (" x " = 0, 0.1, 0.15, 0.2) (cycle between 2.5 and 1.0 V)	particles: 1–2 μm	Ball milling for 8 h + solid state rxn. at 850 °C for 12 h	$\text{Li}_{3-x}\text{Ca}_x\text{Ti}_5\text{O}_{12}$, 0.5C: 166 mAh g^{-1} ; 20C: 123.4 mAh g^{-1}	$\text{Li}_{3-x}\text{Ca}_x\text{Ti}_5\text{O}_{12}$, 162.4, 148.8, and 138.7 mAh g^{-1} after 100 cycles at 1C, 5 C, and 10C, respectively.	30
	$\text{Li}_{4-x}\text{Ca}_x\text{Ti}_5\text{O}_{12}$ (" x " = 0.1) (cycle between 2.5 and 1.0 V)	Nanospheres: 100–200 nm	Solvothermal at 180 °C for 16 h + anneal at 600 °C for 8 h	158 mAh/g capacity at 10C	10 C: retained at 155.1 mAh g^{-1} after 1000 cycles	29
Mg	Mg-doped LTO (cycle between 2.5 V and 0.5 V)	Particles: 30–40 nm	Hydrothermal: 130 °C for 12 h + anneal at 600 °C for 5 h	50C: 156 mAh/g	After 100 cycles, at 50 C: 115 mAh/g	2
Zn	$\text{Li}_{3.95}\text{Zn}_{0.05}\text{Ti}_5\text{O}_{12}$ (cycle between 2.5 and 1.0 V)	Nanosheets: several nanometers in thickness	Hydrothermal: 180 °C for 24 h + anneal at 600 °C for 10 h	10C: 122 mAh/g	10C: 117.4 mAh/g after 20 cycles	54
Sr	$\text{Li}_{4-x}\text{Sr}_x\text{Ti}_5\text{O}_{12}$ (" x " = 0, 0.01, 0.02, 0.03) (cycle between 2.5 and 1.0 V)	Particles: 200 nm	Ball milling for 10 h + solid state rxn. at 850 °C for 18 h in air	" x " = 0.02, at 5C: 104 mAh/g	" x " = 0.02, at 5C: 8.8% capacity loss after 100 cycles	55
Ni	$\text{Li}_{4-x}\text{Ni}_x\text{Ti}_5\text{O}_{12}$ (" x " = 0, 0.025, 0.05 and 0.075) (cycle between 2.5 and 1.0 V)	Particles: 100–1000 nm	Ball milling for 0.5 h + solid state rxn. at 800 °C for 4 h	" x " = 0.15; at 5C: 72 mAh/g		56
Fe	$\text{Li}_{4-x}\text{Fe}_x\text{Ti}_5\text{O}_{12}$ /MWCNT (" x " = 0, 0.05, 0.1, 0.15) (cycle between 2.5 and 1.0 V)	Particles: hundreds of nanometers	Ball milling for 0.5 h + solid state rxn. at 800 °C for 4 h	" x " = 0.1, at 5C: 100 mAh/g; 10C: 57 mAh/g	$\text{Li}_{3.8}\text{Fe}_{0.3}\text{Ti}_{4.9}\text{O}_{12}$ /MWNT after 200 cycles, at 10C, 117% retention	3

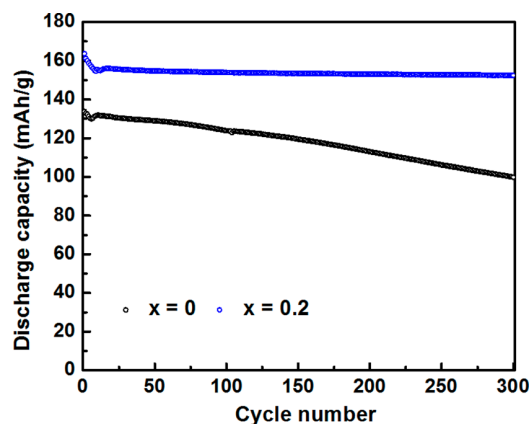


Figure 10. Cycling performance of the Ca-doped $\text{Li}_{4-x}\text{Ca}_x\text{Ti}_5\text{O}_{12}$ (" x " = 0.0 and 0.2) based electrodes at a 20C discharge rate.

(1.718 V, 2229 mA/g), (1.735 V, 2175 mA/g), and (1.706 V, 2637 mA/g). The shoulder peak present at 1.47 V for " x " = 0.1 and " x " = 0.15 electrodes was consistent with the formation of the LiTiO_2 phase from the rutile TiO_2 impurity phase,^{51,52} as determined from the refinement of the relevant XRD profile, illustrated in Figure S1. The " x " = 0.2 material demonstrated the smallest ΔE_p , which was 0.262 V as compared with 0.330 and 0.30 V for the " x " = 0.15 and 0.1 electrodes, respectively, thereby indicating the highest electrochemical reversibility and lowest polarization among all of the doped samples tested. These findings are consistent with the fact that this highly doped, " x " = 0.2 sample delivered the highest discharge capacity under all of the C-rates analyzed.

Electrochemical Impedance Spectroscopy (EIS). To gain insight into the reaction kinetics in the cells and the effect of different doping levels upon charge transfer (R_{ct}) and the effective transfer of Li ions (D_{Li^+}), EIS data were acquired at various states of charge (SOC), including the pristine stage before cycling (Figure 11b and Figure S5c), the full lithiation state in cycle 50 (Figure 11c and Figure S5d), as well as the full delithiation state in cycle 50 (Figure 11d and Figure S5e). The equivalent electrical circuits used to fit all of the EIS spectra are highlighted in Figure S10. In the pristine state, all of the cells with the Ca-doped electrodes demonstrated a similar charge transfer behavior with a measured resistance, ranging from 12 to 17 ohms, i.e., much less than the charge transfer resistance (22 ohms) observed for the undoped LTO-containing cells. These results are indicative of favorable charge transfer behavior for the Ca-doped LTO-containing cells. In cycle 50, after full lithiation, the charge transfer impedance of all of the cells decreased to a similar value, i.e., 5–6 ohms, because the lithiated phase, $\text{Li}_7\text{Ti}_5\text{O}_{12}$, is highly electronically conductive.⁵³ After charging back to the delithiated state, the charge transfer resistance of the undoped along with their successively increasingly doped counterparts increased to 15.7, 6.8, 6.2, and 5.3 ohms, respectively, which evinced a similar trend as with the pristine state. In effect, the undoped LTO materials were found to be the least conductive. The corresponding R_{ct} values are listed in Table S4.

The effective lithium-ion diffusion coefficient (D_{Li^+}) was determined from the fit based upon eq 1, in which R is the gas constant, T is the absolute temperature, A is the contact area of the electrode, n is the number of electrons per molecule, F is the Faraday constant, C is the concentration of Li^+ ions, and σ is the Warburg coefficient associated with the real part of the

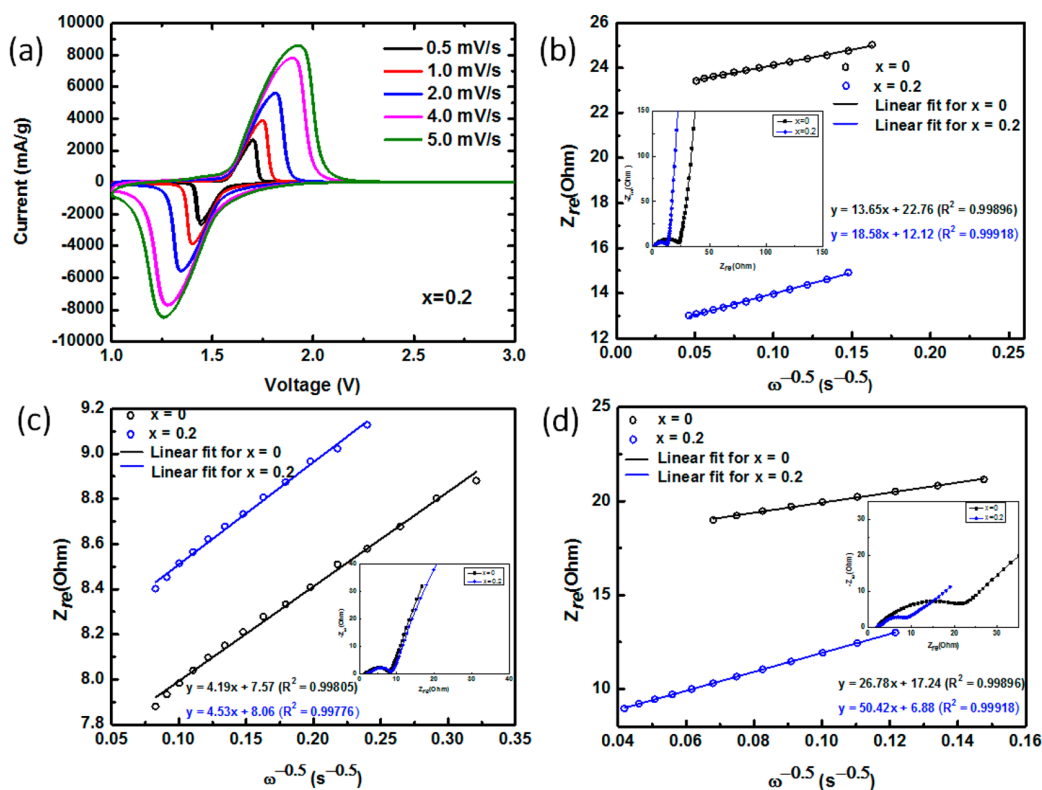


Figure 11. (a) Cyclic voltammograms for “ x ” = 0.2 Ca-doped $\text{Li}_{4-x}\text{Ca}_x\text{Ti}_5\text{O}_{12}$ based electrodes as a function of the scan rate from 0.5 to 5.0 mV/s, as well as the linear fit of the Warburg region from AC impedance with the inset of the Nyquist plot shown for “ x ” = 0.2 and undoped $\text{Li}_4\text{Ti}_5\text{O}_{12}$ electrodes (b) before cycling, (c) after full lithiation, and (d) after full delithiation in cycle 50.

impedance in the low-frequency region (Figure 11b–d and Figure S5c–e), with ω as the angular frequency in eq 2.

$$D_{\text{Li}^+} = (R^2 T^2) / (2A^2 n^4 F^4 C^2 \sigma^2) \quad (1)$$

$$Z_{\text{re}} \propto \sigma \omega^{-1/2} \quad (2)$$

In the pristine state, the linear fits (Figure 11b and Figure S5c) from Z_{re} as a function of $\omega^{-1/2}$ curves of the Warburg region in AC impedance spectra gave rise to the smallest slope for the undoped electrode. The associated results for the effective lithium-ion diffusion coefficients are 6.2×10^{-12} , 2.8×10^{-12} , 4.2×10^{-12} , and 3.2×10^{-12} $\text{cm}^2 \text{s}^{-1}$ for samples containing “ x ” = 0, 0.1, 0.15, and 0.2, respectively. In cycle 50, after full lithiation (Figure 11c and Figure S5d), all of the diffusion coefficients increased for all four of the samples analyzed. Relatively similar effective Li^+ -ion diffusion coefficients are demonstrated among all three of the Ca doped materials analyzed, with the undoped “ x ” = 0 sample possessing a slightly faster Li^+ -ion diffusion rate of 6.1×10^{-11} $\text{cm}^2 \text{s}^{-1}$. By charging back to the delithiated phase (Figure 11d and Figure S5e), the associated results for the effective lithium-ion diffusion coefficients were noted to be 1.5×10^{-12} , 9.7×10^{-13} , 1.1×10^{-13} , and 4.6×10^{-13} $\text{cm}^2 \text{s}^{-1}$ for samples containing “ x ” = 0, 0.1, 0.15, and 0.2, respectively. It is clear that at all various SOC, all of the Ca-doped LTO materials evinced a slower ion diffusion rate as compared with that of their undoped analogue, a finding consistent with the DFT calculations. All of these data suggest that the Ca dopants were preferably located at the $[\text{Li}]_{8a}$ site, thereby implying the addition of a chemically induced impedance to the intrinsic Li^+ -ion diffusion pathway within these modified systems.

4. CONCLUSIONS

A series of doped 3D “flower-like” $\text{Li}_{4-x}\text{Ca}_x\text{Ti}_5\text{O}_{12}$ ($x = 0, 0.1, 0.15, \text{ and } 0.2$) samples has been successfully prepared by using a simple and reproducible hydrothermal reaction coupled with a short calcination process. The TEM, SEM, and EDS mapping data have suggested that the calcium incorporation was homogeneous within the LTO motif without perceptibly altering the “flower-like” structure. XRD results indicate that all of the Ca-doped samples retained a spinel crystal structure and gave rise to a shift of the (111) peak to lower angles, with the “ x ” = 0.2 sample showing the largest shift detected, thereby indicating the presence of lattice expansion after Ca-ion doping.

Such a lattice expansion was also apparent in the DFT calculations, an observation ascribed to substitution of the doped Ca^{2+} ions with analogous Li^+ ions at the site of LTO. Such data are different from those reported on Ca-doped LTO spheres in previous DFT studies led by Zhang et al.,^{28,40,41} which postulated Ca localization at the $[\text{Li}]_{16d}$ site within a triclinic model structure. Within our system, our DFT-optimized model of Ca-doped LTO fits the measured XRD pattern very well. Both DFT calculations and the subsequent EIS data have confirmed that the Ca dopants localized at the $[\text{Li}]_{8a}$ site likely increased the Li-ion diffusion impedance along the 8a–16c–8a pathway.

XPS data revealed that the amount of Ti^{3+} rose dramatically within the “ x ” = 0.2 sample, due to an induced charge compensation effect, thereby leading to favorably enhanced electronic conductivity and, therefore, considerably better electrochemical properties. This assertion is also supported by the PDOS results from DFT calculations, which show that the Ca-ion doping significantly decreases the band gap and thereby

enhances the electronic conductivity, due to the partial reduction of Ti^{4+} to Ti^{3+} species within Ca-doped LTO. That is, our collective data suggest that although Ca dopants can potentially block the Li^+ pathway, they render the doped LTO as intrinsically more electron conductive by affecting the underlying electronic band structure.

Overall, our collective experimental and theoretical characterization efforts have confirmed that the improved electrochemical performance of the Ca-doped LTO sample possessing a “ x ” = 0.2 doping ratio, could mainly be ascribed to an enhanced electronic conductivity, as opposed to an increase in the Li-ion diffusion rate, induced by the presence of Ca dopants. Specifically, measured capacities of 163, 151, 143, and 75 mAh/g were observed under discharge rates of 0.2C, 20C, 40C, and 100C, at cycles 50, 60, 70, and 80, respectively. This doped material also demonstrated a high cycling stability, with capacity retention values of 94% and 92% for cycle 100 and 300, respectively, at a very high discharge rate of 20C.

■ ASSOCIATED CONTENT

Supporting Information

The Supporting Information is available free of charge on the ACS Publications website at DOI: 10.1021/acs.chemmater.7b03847.

Additional Rietveld refinement results, electrochemical characterization data, and theoretical insights into all of the samples analyzed, including control samples (PDF)

■ AUTHOR INFORMATION

Corresponding Authors

*A. C. Marschilok. Email: amy.marschilok@stonybrook.edu.

*S. S. Wong. Email: stanislaus.wong@stonybrook.edu; sswong@bnl.gov.

ORCID

Lei Wang: 0000-0002-6348-8344

Eric A. Stach: 0000-0002-3366-2153

Esther S. Takeuchi: 0000-0001-8518-1047

Ping Liu: 0000-0001-8363-070X

Amy C. Marschilok: 0000-0001-9174-0474

Stanislaus S. Wong: 0000-0001-7351-0739

Author Contributions

These authors contributed equally to this work.

Notes

The authors declare no competing financial interest.

■ ACKNOWLEDGMENTS

All of the work described in these studies was funded as part of the Center for Mesoscale Transport Properties (m2M), an Energy Frontier Research Center supported by the U.S. Department of Energy, Office of Science, Basic Energy Sciences, under award #DE-SC0012673. Experimental research characterization and theoretical DFT calculations were carried out in part at the Center for Functional Nanomaterials, Brookhaven National Laboratory, an Office of Science User Facility, which is supported by the U.S. Department of Energy, Office of Basic Energy Sciences, under Contract No. DE-SC0012704.

■ REFERENCES

(1) Yi, T.-F.; Xie, Y.; Jiang, L.-J.; Shu, J.; Yue, C.-B.; Zhou, A.-N.; Ye, M.-F. Advanced Electrochemical Properties of Mo-Doped $Li_4Ti_5O_{12}$

Anode Material for Power Lithium Ion Battery. *RSC Adv.* **2012**, *2*, 3541–3547.

(2) Wang, W.; Jiang, B.; Xiong, W. Y.; Wang, Z.; Jiao, S. Q. A Nanoparticle Mg-Doped $Li_4Ti_5O_{12}$ for High Rate Lithium-Ion Batteries. *Electrochim. Acta* **2013**, *114*, 198–204.

(3) Lin, C. F.; Fan, X. Y.; Xin, Y. L.; Cheng, F. Q.; Lai, M. O.; Zhou, H. H.; Lu, L. $Li_4Ti_5O_{12}$ -Based Anode Materials with Low Working Potentials, High Rate Capabilities and High Cyclability for High-Power Lithium-Ion Batteries: A Synergistic Effect of Doping, Incorporating a Conductive Phase and Reducing the Particle Size. *J. Mater. Chem. A* **2014**, *2*, 9982–9993.

(4) Abureden, S.; Hassan, F. M.; Lui, G.; Ahn, W.; Sy, S.; Yu, A. P.; Chen, Z. W. Multigrain Electrospun Nickel Doped Lithium Titanate Nanofibers with High Power Lithium Ion Storage. *J. Mater. Chem. A* **2016**, *4*, 12638–12647.

(5) Ma, J.; Wang, C.; Wroblewski, S. Kinetic Characteristics of Mixed Conductive Electrodes for Lithium Ion Batteries. *J. Power Sources* **2007**, *164*, 849–856.

(6) Kavan, L.; Procházka, J.; Spitzler, T. M.; Kalbáč, M.; Zukalová, M. t.; Drezek, T.; Grätzel, M. Li Insertion into $Li_4Ti_5O_{12}$ (Spinel). *J. Electrochem. Soc.* **2003**, *150*, A1000.

(7) Jiang, Y. M.; Wang, K. X.; Zhang, H. J.; Wang, J. F.; Chen, J. S. Hierarchical $Li_4Ti_5O_{12}/TiO_2$ Composite Tubes with Regular Structural Imperfection for Lithium Ion Storage. *Sci. Rep.* **2013**, *3*, 3490.

(8) Lim, J.; Choi, E.; Mathew, V.; Kim, D.; Ahn, D.; Gim, J.; Kang, S. H.; Kim, J. Enhanced High-Rate Performance of $Li_4Ti_5O_{12}$ Nanoparticles for Rechargeable Li-Ion Batteries. *J. Electrochem. Soc.* **2011**, *158*, A275–A280.

(9) Sun, L.; Wang, J. P.; Jiang, K. L.; Fan, S. S. Mesoporous $Li_4Ti_5O_{12}$ Nanoclusters as High Performance Negative Electrodes for Lithium Ion Batteries. *J. Power Sources* **2014**, *248*, 265–272.

(10) Shen, L. F.; Uchaker, E.; Zhang, X. G.; Cao, G. Z. Hydrogenated $Li_4Ti_5O_{12}$ Nanowire Arrays for High Rate Lithium Ion Batteries. *Adv. Mater.* **2012**, *24*, 6502–6506.

(11) Liu, J.; Song, K. P.; van Aken, P. A.; Maier, J.; Yu, Y. Self-Supported $Li_4Ti_5O_{12}$ -C Nanotube Arrays as High-Rate and Long-Life Anode Materials for Flexible Li-Ion Batteries. *Nano Lett.* **2014**, *14*, 2597–2603.

(12) Tang, Y. F.; Yang, L.; Fang, S. H.; Qiu, Z. $Li_4Ti_5O_{12}$ Hollow Microspheres Assembled by Nanosheets as an Anode Material for High-Rate Lithium Ion Batteries. *Electrochim. Acta* **2009**, *54*, 6244–6249.

(13) Chen, J. Z.; Yang, L.; Fang, S. H.; Tang, Y. F. Synthesis of Sawtooth-Like $Li_4Ti_5O_{12}$ Nanosheets as Anode Materials for Li-Ion Batteries. *Electrochim. Acta* **2010**, *55*, 6596–6600.

(14) Kong, D.; Ren, W.; Luo, Y.; Yang, Y.; Cheng, C. Scalable Synthesis of Graphene-Wrapped $Li_4Ti_5O_{12}$ Dandelion-Like Microspheres for Lithium-Ion Batteries with Excellent Rate Capability and Long-Cycle Life. *J. Mater. Chem. A* **2014**, *2*, 20221–20230.

(15) Ni, H. F.; Fan, L. Z. Nano- $Li_4Ti_5O_{12}$ Anchored on Carbon Nanotubes by Liquid Phase Deposition as Anode Material for High Rate Lithium-Ion Batteries. *J. Power Sources* **2012**, *214*, 195–199.

(16) Shen, L.; Zhang, X.; Uchaker, E.; Yuan, C.; Cao, G. $Li_4Ti_5O_{12}$ Nanoparticles Embedded in a Mesoporous Carbon Matrix as a Superior Anode Material for High Rate Lithium Ion Batteries. *Adv. Energy Mater.* **2012**, *2*, 691–698.

(17) Xu, G. B.; Li, W.; Yang, L. W.; Wei, X. L.; Ding, J. W.; Zhong, J. X.; Chu, P. K. Highly-Crystalline Ultrathin $Li_4Ti_5O_{12}$ Nanosheets Decorated with Silver Nanocrystals as a High-Performance Anode Material for Lithium Ion Batteries. *J. Power Sources* **2015**, *276*, 247–254.

(18) Ouyang, C. Y.; Zhong, Z. Y.; Lei, M. S. Ab Initio Studies of Structural and Electronic Properties of $Li_4Ti_5O_{12}$ Spinel. *Electrochem. Commun.* **2007**, *9*, 1107–1112.

(19) Zhu, G.-N.; Wang, Y.-G.; Xia, Y.-Y. Ti-Based Compounds as Anode Materials for Li-Ion Batteries. *Energy Environ. Sci.* **2012**, *5*, 6652.

- (20) Yi, T.-F.; Jiang, L.-J.; Shu, J.; Yue, C.-B.; Zhu, R.-S.; Qiao, H.-B. Recent Development and Application of $\text{Li}_4\text{Ti}_5\text{O}_{12}$ as Anode Material of Lithium Ion Battery. *J. Phys. Chem. Solids* **2010**, *71*, 1236–1242.
- (21) Goodenough, J. B.; Kim, Y. Challenges for Rechargeable Li Batteries. *Chem. Mater.* **2010**, *22*, 587–603.
- (22) Wilkening, M.; Amade, R.; Iwaniak, W.; Heitjans, P. Ultraslow Li Diffusion in Spinel-Type Structured $\text{Li}_4\text{Ti}_5\text{O}_{12}$ - a Comparison of Results from Solid State NMR and Impedance Spectroscopy. *Phys. Chem. Chem. Phys.* **2007**, *9*, 1239–46.
- (23) Zhang, Q. Y.; Li, X. Recent Developments in the Doped- $\text{Li}_4\text{Ti}_5\text{O}_{12}$ Anode Materials of Lithium-Ion Batteries for Improving the Rate Capability. *Int. J. Electrochem. Sci.* **2013**, *8*, 6449–6456.
- (24) Yi, T. F.; Xie, Y.; Shu, J.; Wang, Z. H.; Yue, C. B.; Zhu, R. S.; Qiao, H. B. Structure and Electrochemical Performance of Niobium-Substituted Spinel Lithium Titanium Oxide Synthesized by Solid-State Method. *J. Electrochem. Soc.* **2011**, *158*, A266–A274.
- (25) Zhao, Y.; Li, J.; Li, Z.; Yang, K.; Gao, F. Pr-Modified $\text{Li}_4\text{Ti}_5\text{O}_{12}$ Nanofibers as an Anode Material for Lithium-Ion Batteries with Outstanding Cycling Performance and Rate Performance. *Ionics* **2016**, *1–9*, 597–605.
- (26) Nie, S.; Li, C.; Peng, H.; Li, G.; Chen, K. Ti^{3+} Self-Doped $\text{Li}_4\text{Ti}_5\text{O}_{12}$ Nanosheets as Anode Materials for High Performance Lithium Ion Batteries. *RSC Adv.* **2015**, *5*, 23278–23282.
- (27) Wang, B. F.; Wang, J. S.; Cao, J.; Ge, H. H.; Tang, Y. F. Nitrogen-Doped $\text{Li}_4\text{Ti}_5\text{O}_{12}$ Nanosheets with Enhanced Lithium Storage Properties. *J. Power Sources* **2014**, *266*, 150–154.
- (28) Zhang, Q. Y.; Verde, M. G.; Seo, J. K.; Li, X.; Meng, Y. S. Structural and Electrochemical Properties of Gd-Doped $\text{Li}_4\text{Ti}_5\text{O}_{12}$ as Anode Material with Improved Rate Capability for Lithium-Ion Batteries. *J. Power Sources* **2015**, *280*, 355–362.
- (29) Zhang, Q. Y.; Zhang, S. H.; Ning, F. H.; Lu, X.; Liu, Y.; Nie, L. H.; Ouyang, C. Y.; Zhang, L. Z. Calcium Doping of Lithium Titanium Oxide Nanospheres: A Combined First-Principles and Experimental Study. *Energy Technol.* **2017**, *5*, 539–543.
- (30) Zhang, Q. Y.; Zhang, C. L.; Li, B.; Kang, S. F.; Li, X.; Wang, Y. G. Preparation and Electrochemical Properties of Ca-Doped $\text{Li}_4\text{Ti}_5\text{O}_{12}$ as Anode Materials in Lithium-Ion Battery. *Electrochim. Acta* **2013**, *98*, 146–152.
- (31) Setiawan, D.; Subhan, A.; Saptari, S. A. Ca-Doped LTO Using Waste Eggshells as Ca Source to Improve the Discharge Capacity of Anode Material for Lithium-Ion Battery. *AIP Conf. Proc.* **2016**, *1862*, 030073.
- (32) Zhang, Q.; Li, X. Improving the Energy Density of Ca-Doped $\text{Li}_4\text{Ti}_5\text{O}_{12}$ through Discharging to 0 V Cut-Off Voltage. *Int. J. Electrochem. Sci.* **2013**, *8*, 9734–9740.
- (33) Wang, L.; Zhang, Y. M.; Scofield, M. E.; Yue, S. Y.; McBean, C.; Marschilok, A. C.; Takeuchi, K. J.; Takeuchi, E. S.; Wong, S. S. Enhanced Performance of “Flower-Like” $\text{Li}_4\text{Ti}_5\text{O}_{12}$ Motifs as Anode Materials for High-Rate Lithium-Ion Batteries. *ChemSusChem* **2015**, *8*, 3304–3313.
- (34) Xia, H.; Luo, Z. T.; Xie, J. P. Nanostructured Lithium Titanate and Lithium Titanate/Carbon Nanocomposite as Anode Materials for Advanced Lithium-Ion Batteries. *Nanotechnol. Rev.* **2014**, *3*, 161–175.
- (35) Kresse, G.; Furthmüller, J. Efficiency of Ab-Initio Total Energy Calculations for Metals and Semiconductors Using a Plane-Wave Basis Set. *Comput. Mater. Sci.* **1996**, *6*, 15–50.
- (36) Blochl, P. E. Projector Augmented-Wave Method. *Phys. Rev. B: Condens. Matter Mater. Phys.* **1994**, *50*, 17953–17979.
- (37) Perdew, J. P.; Burke, K.; Ernzerhof, M. Generalized Gradient Approximation Made Simple. *Phys. Rev. Lett.* **1996**, *77*, 3865–3868.
- (38) Bruix, A.; Rodriguez, J. A.; Ramirez, P. J.; Senanayake, S. D.; Evans, J.; Park, J. B.; Stacchiola, D.; Liu, P.; Hrbek, J.; Illas, F. A New Type of Strong Metal–Support Interaction and the Production of H_2 through the Transformation of Water on Pt/CeO₂(111) and Pt/CeO₂/TiO₂(110) Catalysts. *J. Am. Chem. Soc.* **2012**, *134*, 8968–8974.
- (39) Ziebarth, B.; Klinsmann, M.; Eckl, T.; Elsassner, C. Lithium Diffusion in the Spinel Phase $\text{Li}_4\text{Ti}_5\text{O}_{12}$ and in the Rocksalt Phase $\text{Li}_7\text{Ti}_5\text{O}_{12}$ of Lithium Titanate from First Principles. *Phys. Rev. B: Condens. Matter Mater. Phys.* **2014**, *89*, 174301.
- (40) Verde, M. G.; Baggetto, L.; Balke, N.; Veith, G. M.; Seo, J. K.; Wang, Z. Y.; Meng, Y. S. Elucidating the Phase Transformation of $\text{Li}_4\text{Ti}_5\text{O}_{12}$ Lithiation at the Nanoscale. *ACS Nano* **2016**, *10*, 4312–4321.
- (41) Liu, D. T.; Ouyang, C. Y.; Shu, J.; Jiang, J.; Wang, Z. X.; Chen, L. Q. Theoretical Study of Cation Doping Effect on the Electronic Conductivity of $\text{Li}_4\text{Ti}_5\text{O}_{12}$. *Phys. Status Solidi B* **2006**, *243*, 1835–1841.
- (42) Duan, H.; Li, J.; Du, H. D.; Chiang, S. W.; Xu, C. J.; Duan, W. H.; Kang, F. Y. Tailoring Native Defects and Zinc Impurities in $\text{Li}_4\text{Ti}_5\text{O}_{12}$: Insights from First-Principles Study. *J. Phys. Chem. C* **2015**, *119*, S238–S245.
- (43) Lin, C. F.; Fan, X. Y.; Xin, Y. L.; Cheng, F. Q.; Lai, M. O.; Zhou, H. H.; Lu, L. Monodispersed Mesoporous $\text{Li}_4\text{Ti}_5\text{O}_{12}$ Submicrospheres as Anode Materials for Lithium-Ion Batteries: Morphology and Electrochemical Performances. *Nanoscale* **2014**, *6*, 6651–6660.
- (44) Qian, K.; Tang, L.; Wagemaker, M.; He, Y.-B.; Liu, D.; Li, H.; Shi, R.; Li, B.; Kang, F. A Facile Surface Reconstruction Mechanism toward Better Electrochemical Performance of $\text{Li}_4\text{Ti}_5\text{O}_{12}$ in Lithium-Ion Battery. *Adv. Sci.* **2017**, *4*, 1700205.
- (45) Borghols, W. J. H.; Wagemaker, M.; Lafont, U.; Kelder, E. M.; Mulder, F. M. Size Effects in the $\text{Li}_{4+x}\text{Ti}_5\text{O}_{12}$ Spinel. *J. Am. Chem. Soc.* **2009**, *131*, 17786–17792.
- (46) Deng, J. Q.; Lu, Z. G.; Belharouak, I.; Amine, K.; Chung, C. Y. Preparation and Electrochemical Properties of $\text{Li}_4\text{Ti}_5\text{O}_{12}$ Thin Film Electrodes by Pulsed Laser Deposition. *J. Power Sources* **2009**, *193*, 816–821.
- (47) Ganapathy, S.; Wagemaker, M. Nanosize Storage Properties in Spinel $\text{Li}_4\text{Ti}_5\text{O}_{12}$ Explained by Anisotropic Surface Lithium Insertion. *ACS Nano* **2012**, *6*, 8702–8712.
- (48) Kim, J.-G.; et al. Zr^{4+} Doping in $\text{Li}_4\text{Ti}_5\text{O}_{12}$ Anode for Lithium-Ion Batteries: Open Li^+ Diffusion Paths through Structural Imperfection. *ChemSusChem* **2014**, *7*, 1451–1457.
- (49) Zhang, Y. Y.; Zhang, C. M.; Lin, Y.; Xiong, D. B.; Wang, D.; Wu, X. Y.; He, D. N. Influence of Sc^{3+} Doping in B-Site on Electrochemical Performance of $\text{Li}_4\text{Ti}_5\text{O}_{12}$ Anode Materials for Lithium-Ion Battery. *J. Power Sources* **2014**, *250*, 50–57.
- (50) Li, Z. Y.; Li, J. L.; Zhao, Y. G.; Yang, K.; Gao, F.; Li, X. Structure and Electrochemical Properties of Sm-Doped $\text{Li}_4\text{Ti}_5\text{O}_{12}$ as Anode Material for Lithium-Ion Batteries. *RSC Adv.* **2016**, *6*, 15492–15500.
- (51) Wang, D.; Choi, D.; Yang, Z.; Viswanathan, V. V.; Nie, Z.; Wang, C.; Song, Y.; Zhang, J.-G.; Liu, J. Synthesis and Li-Ion Insertion Properties of Highly Crystalline Mesoporous Rutile TiO_2 . *Chem. Mater.* **2008**, *20*, 3435.
- (52) Bai, Y.; Liu, Z.; Zhang, N.; Sun, K. One-Pot Synthesis of 3-D Dandelion-Like Architectures Constructed by Rutile TiO_2 Nanorods Grown Along [001] Axis for High-Rate Lithium Ion Batteries. *RSC Adv.* **2015**, *5*, 21285–21289.
- (53) Verde, M. G.; Baggetto, L.; Balke, N.; Veith, G. M.; Seo, J. K.; Wang, Z.; Meng, Y. S. Elucidating the Phase Transformation of $\text{Li}_4\text{Ti}_5\text{O}_{12}$ Lithiation at the Nanoscale. *ACS Nano* **2016**, *10*, 4312–4321.
- (54) Zhang, Z.; Cao, L.; Huang, J.; Zhou, S.; Huang, Y.; Cai, Y. Hydrothermal Synthesis of Zn-Doped $\text{Li}_4\text{Ti}_5\text{O}_{12}$ with Improved High Rate Properties for Lithium Ion Batteries. *Ceram. Int.* **2013**, *39*, 6139–6143.
- (55) Wu, H.; Chang, S.; Liu, X.; Yu, L.; Wang, G.; Cao, D.; Zhang, Y.; Yang, B.; She, P. Sr-Doped $\text{Li}_4\text{Ti}_5\text{O}_{12}$ as the Anode Material for Lithium-Ion Batteries. *Solid State Ionics* **2013**, *232*, 13–18.
- (56) Lin, C.; Lai, M. O.; Lu, L.; Zhou, H.; Xin, Y. Structure and High Rate Performance of Ni^{2+} Doped $\text{Li}_4\text{Ti}_5\text{O}_{12}$ For lithium Ion Battery. *J. Power Sources* **2013**, *244*, 272–279.